Solid Earth Discuss., 5, 1511–1573, 2013
www.solid-earth-discuss.net/5/1511/2013/
doi:10.5194/sed-5-1511-2013

Solid Earth
Discussions
Open Access

The enigmatic Zerelia twin-lakes (Thessaly, Central Greece): two potential meteorite impact Craters

V. J. Dietrich[1], E. Lagios[2], E. Reusser[1], V. Sakkas[2], E. Gartzos[3], and K. Kyriakopoulos[4]

[1]Institute for Geochemistry and Petrology, Swiss Federal Institute of Technology, 8092 Zurich, Switzerland
[2]Department of Geophysics and Geothermics, National and Kapodistrian University of Athens, Panepistimiopolis-Ilissia, 157 84 Athens, Greece
[3]Laboratory of Mineralogy-Geology, Agricultural University of Athens, 118 55 Athens, Greece
[4]Department of Geology and Geoenvironment, Section of Mineralogy and Petrology, National and Kapodistrian University of Athens, Panepistimiopolis-Ilissia, 157 84 Athens, Greece

Received: 31 July 2013 – Accepted: 13 August 2013 – Published: 3 September 2013

Correspondence to: V. J. Dietrich (volker.dietrich@erdw.ethz.ch)

Published by Copernicus Publications on behalf of the European Geosciences Union.

Abstract

Two circular permanent lakes of 150 and 250 m diameter and 6–8 m depth to an unconsolidated muddy bottom occur 250 m apart from each other in the agricultural fields SW of the town of Almiros (Thessaly, central Greece). The age of the lakes is assumed to be Late Pliocene to Early Holocene with a minimum age of approx. 7000 yr BP.

The abundant polymict, quartz-rich carbonate breccia and clasts with a clay rich matrix in the shallow embankments of the lakes show weak stratification but no volcanic structures. The carbonate clasts and particles often display spheroidal shapes and consist of calcite aggregates with feathery, arborescent, variolitic to micro-sparitic textures and spheroidal fabrics, recrystallized and deformed glass-shaped fragments, calcite globules in quartz; thus indications of possible carbonate melting, quenching and devitrification. The carbonatic matrix includes small xenomorphic phases, such as chromspinel, zircon with blurred granular and skeletal textures, skeletal rutile and ilmenite, which are interpreted as relicts of partial melting and quenching under high temperatures of 1240–1800 °C. Only a few quartz fragments exhibit indistinct planar fractures. In several cases they include exotic Al-Si- and sulfur bearing Fe-phases, < 1–10 µm as globules.

The modeled "Residual Gravity" profiles through the lakes indicate negative gravity anomalies of bowl-type structures down to 150 m for the eastern lake and down to 250 m for the larger western lake. Several hypotheses can be drawn upon to explain the origin of these enigmatic twin-lakes: (a) Maar-type volcanic craters; (b) hydrothermal or CO_2/hydrocarbon gas explosion craters; (c) and (d) doline holes due to karstification; or (e) small meteorite impact craters, the latter being a plausible explanation due to geologic, petrologic, and geophysical evidence.

The morphology and dimensions of the lakes as well as the density contrast tomography of the bedrock favor a meteorite impact hypothesis of a projectile, which may has split into two fragments before reaching the surface.

SED
5, 1511–1573, 2013

1 Introduction

The Magoula Zerelia twin-lakes are located in the agricultural fields SW of the town of Almiros in Thessaly. This picturesque site is known as the prehistoric Magoula Zerelia settlement on the hill between the two lakes (Fig. 1), which was occupied from the Middle Neolithic period until Late Bronze Age (Reinders and Bottema, 1983; Reinders, 2004). According to an old story (Theocharis, 1973) "the temple of Athena Itona is situated in one of the two lakes and only visible when the lake falls dry", which only happened in 1980 after the M_w = 6.5 strong earthquake, located approx. 6 km north of the lakes (Papazachros et al., 1983). On the high-resolution Google earth image the lakes stand out by their morphological shape and indistinct halos, which appear as remnants of shallow walls covered with unusual rock debris. Unfortunately no geological outcrops of the bedrock are present within the proximal vicinity.

Reconnaissance sampling and first petrographic studies of the collected rock material in 2008 (Dietrich and Gartzos, 2009) revealed the possibility to interpret the formation of the lakes as due to a meteorite impact. Previously, the origin of the lakes has been assumed as result of maar-type volcanic or CO_2 eruptions on the basis of the existence of small Pliocene to Pleistocene trachyandesitic volcanic centers in the wider area (Marinou, 1963; Marinos and Papakis, 1965; Innocenti et al., 1979).

The ages of the lakes can only be estimated from their well preserved morphological character and thus may be bracketed between Late Pliocene to Early Holocene and approximately 7000 yr BP; the latter age according to the Middle Neolithic settlement on the hill between the two lakes (Fig. 1). Radiocarbon dating of a palynological sample taken from a boring at 10 m depth below the bottom of the larger lake 2 yielded an age of 1440 ± 60 yr BP (Reinders and Bottema, 1983; Reinders, 1988). Two of us (V. D. and E. G.) took several 0.35 to 0.75 cm long piston cores in the fall of 2009 from the bottom of the lakes. Caesium and lead isotope dating yielded sedimentation rates between 0.44 and 0.50 cm yr^{-1} for the larger lake ZLW (Keller, 2010). Providing a constant rate

SED
5, 1511–1573, 2013

of sedimentation of 0.5 m yr^{-1} the lake 2 could have had an original maximal depth between 50 and 60 m.

Therefore, geophysical investigations in 2010 were undertaken using magnetic and gravity measurements to define the bedrock structure of the lakes (e.g. diatreme vs. bowl structure) and to find an indication of relict pieces of projectiles at depth. The goal of this work is a detailed petrographic, mineralogical, chemical description of the unusual rock material covering the walls of the lakes in order to elucidate their enigmatic character.

However, it should be noted, that up to now, no trace of the projectile (stone or iron meteorite) has been found.

2 Geological setting

The geological setting (lithologies and stratigraphy) of the bedrock of the lakes can only be based on the variety of detrital rocks on the surface of the agricultural fields around the lakes and within the regional framework of the Almiros plain. The closest outcrops of the Upper Neogene and Quaternary occur in the riverbeds and banks west of the Almiros village 1.5–2 km north of the lakes. The Quaternary in the Almiros plain reaches several meters depending on the topography, covering Neogene and Mesozoic formations below (Geological maps of Greece 1 : 50 000: sheet Anavra, Marinos et al., 1957 and sheet Almiros, Marinos et al., 1962). For this reason, a geological profile through the bedrock of the lakes is highly speculative, and only a hypothetical model can be presented at the end of the discussion on the basis of the geophysical data and the lithologies encountered in the breccia. In general, the form and shapes of the residual negative gravity anomalies bowl-type bedrock structures of the lakes down to at least 100 m.

Remarkable is the rather asymmetric distribution of the brecciated material in the slopes around the larger westerly lake ZLW. While this material is almost absent in the

SED
5, 1511–1573, 2013

northern rim, is covers entirely the southern slopes. For the smaller easterly lake ZLE such an asymmetric distribution is not clear due to the dense vegetation.

The most abundant sedimentary detrital rocks in the surface of the neighboring agricultural fields around the lakes are undeformed Cretaceous limestones besides few radiolarian cherts and very rare serpentinites. This is particularly the case in the northern vicinity of the lakes and in the Neolithic hillside between the lakes (Fig. 1).

The structural and stratigraphic situation of the bedrock can ~~only~~ be correlated with the highly complex "Alpine tectonics" of the neighboring Othris Mountains (Fig. 2a and b), which consist of faulted thrust sheets variable in size with dimensions from a few hundred meters to several kilometers, vertically and horizontally. The "Sub-Pelagonian Othrys" group comprises lithologies of Triassic to Cretaceous shallow-water platform carbonates, pelagic limestones, shales and cherts, as well as "flysch-type" turbiditic sandstones and fragmental carbonates. In addition, irregular disseminated sheets and lenses of ophiolitic mélange and ultramafic bodies (review in Smith et al., 1975; Pe-Piper and Piper 1989; Robertson and Varnavas, 1993) are present.

The Mesozoic formations are covered in general by Neogene shallow marine to lacustrine sediments consisting of cemented marly limestones, sandstones and gravel interlayered with reddish clayey material and calcareous pebbles. These sediments of Pliocene-Lower Pleistocene age are characterized by frequent lateral and vertical facies variations and reach 20 to 40 m thickness in the Almiros plain. Brownish-reddish breccias and sandstones ("Almiros formation", Caputo, 1996) occur in the lowermost stratigraphic levels, along the northern borders of the Almiros plain. Towards south they grade into white to yellowish marls interbedded with fine-grained clastic fluvio-lacustrine sediments. In the uppermost levels volcano-clastic debris has been found (Caputo, 1990), which has been derived from the Pleistocene 1.4 ± 0.1 Ma dated basaltic Thive volcano (Innocenti et al., 1979). These sediments are unconformably overlain in places by poorly cemented "Red Bed type" clastic sediments of variable grain size, indicating a special "climatic event" of unknown age. However, this uncon-

SED
5, 1511–1573, 2013

solidated red clastic formation might not be attributed to any paleoclimatic change or desert situation but rather to regional drainage situations (Sheldon, 2005).

The soil as well as the slopes around the smaller eastern lake ZLE (Fig. 2a) is composed of white to yellowish, partly ~~carbonate~~ breccias with grain sizes from sand to clasts of several centimeters in size. All rock pieces exhibit irregular angular to subrounded shapes, full of cavities, disseminated calcite veins and contain few but distinct fragments of reddish radiolarian cherts. Fragments of limestones, cherts, shales and schists, similar to those of the surrounding Mesozoic basement formations, are very rare.

In contrast, the soil and the southern slopes of the larger western lake ZLW (Fig. 2b) is mainly made up of yellowish to orange polymict carbonate breccias with grain sizes from sand to clasts of several centimeters in diameter. Occasional bigger blocks reach sizes of 10 to 20 cm (Fig. 3a). These chaotic unconsolidated carbonatic and marly clastic sediments crop out in two cross sections in the southern and northern walls of lake 2 (sampling points SP1 and SP2 in Figs. 1, 3a and b) showing any signs of sorting and stratification. At first glance, these outcrops could resemble either “saprolitic” horizons of bedrock or lenses of deeply weathered, kaolinized marls and shales. However, the appearance of reddish chert and quartz fragments as well as polymict breccias reveals a different origin. Neither typical Mesozoic and Neogene limestone fragments nor plutonic or volcanic material including ultramafic mantle inclusions are present.

Remarkable is the rather asymmetric distribution of the brecciated material in the slopes around lake 2. While this material is almost absent in the northern rim, is covers entirely the southern slopes. For the smaller easterly lake 1 such an asymmetric distribution is not clear due to the dense vegetation.

In the southwestern part of the embankment of the easterly lake ZLE a 7 m deep and 1 m wide trench TRE (Figs. 1 and 3e), not touching the bedrock, has been excavated during 27 June 2013. The entire formation showed an unconsolidated sequence of detrital rock fragments in variable size from millimeter to centimeter and clay matrix supported. The first 10 cm consist of humus; surficial roots and plants penetrate

SED
5, 1511–1573, 2013

the upper 1–2 m. The whole sequence from 1–7 m is made up of indistinct layers, indicated by horizontal variation of mainly reddish, brown, white, and grey colors. The matrix is consists mainly of clay and marls. Small, up to a few centimeters, calcareous fragments comprise the predominant material; a piece of 20 cm × 30 cm found at the depth of 5 m. In places altered blocks of intercalated white marly limestones occur. The unconsolidated rock sequence could be designated as mudstones, in parts as packstones. Fragments of limestones, sandstones and metamorphic rocks (cherts, schists, and serpentinites) are missing throughout the entire sequence. No calcite vein network is present. However, high humidity in all parts ~~leads to~~ the semi-plastic behavior of the rock sequence, providing the trench to break down.

The difference in colors indicates the existence of layers due to periodic climatic changes and debris input during storms. Thus the sequence exhibits the typical characteristics of lake sedimentation and represents an older border part of the lake with a larger diameter than today. An almost identical rock sequence has been found in the 1 m wide and 8.5 m deep trench (TRW) in the southeastern shore of the large lake ZLW (Fig. 1).

3 Petrography of breccias and clasts in the embankment around the Zerelia lakes (for analytical procedures see Appendix)

3.1 Polymict carbonate breccias and clasts

Two lithic yellowish to orange breccia types occur as abundant detritus in the slopes around the larger western lake ZLW, whereas around the smaller eastern lake ZLE only one breccia type has been recognized: The most common "*type A breccia*" comprises rock fragments, which are cemented by a non-porous carbonatic feathery, arborescent and variolitic textured matrix (Fig. 3c). The amount of angular to subrounded fragments varies from a few percent to a maximum of approximately 50 %, the main components with a random distribution of all sizes from µm–cm are quartz, cherts, and red radio-

SED
5, 1511–1573, 2013

larian cherts. Grey and red dense cherts and radiolarian cherts are the most abundant rock fragments from micron to cm in size. In most cases, they are undeformed, only fractured and partly internally brecciated. Quartz fragments show all stages of brecciation from fracturing to disintegration and contain in some cases globules of calcite. In addition, small fragments of accessory minerals, such as ilmenite, rutile, zircon, apatite, magnetite, different phases of spinel as well as recrystallized ~~glass shaped~~ fragments are present in the groundmass. Neither fragments of limestones nor schists from the bedrock Mesozoic or Neogene formations have been recognized in the type A breccia. According to the depositional fabrics, this type of lithic clastic rocks could be classified as "wackestone" (Dunham, 1962).

A less common yellow to light orange, non porous polymict breccia (*type B breccia*, Figs. 3d, 4e and f), also rich in quartz and chert fragments, angular to slightly subrounded, is cemented by a carbonatic cryptocrystalline to micro-sparitic matrix, densely packed with carbonatic "spheres" and "spheroidal particles" of 0.1 to 1 mm dimensions. Only this type occurs in the slopes of the eastern lake. However compared to type A breccia, the type B breccia contains subordinate fragments of schists, serpentinite, diabase and micro-sparitic calcite patches, which can be recognized as recrystallized limestones, and shell fragments. The spheroidal particles can be loosely packed or partly coagulated. In several cases, euhedral and fragmented quartz crystals contain inclusions of calcite, dolomite, apatite, mica, plagioclase, and fayalite as well as not well-identified globules of Al-Si-Fe phases and fluid inclusions. In the classification of Dunham, these breccias could be designated as "packstone and grainstone".

3.2 Spheroidal carbonate clasts, spheres and spheroidal particles

3.2.1 Spheroidal carbonate clasts

~~Often,~~ centimeter-sized feathery carbonatic clasts have cauliflower shapes and are infiltrated by a tiny network of calcite veins. Smaller, spheroidal shaped "lapilli- like" carbonate clasts of millimeters to centimeters in size, resembling "septarian concre-

SED
5, 1511–1573, 2013

tions", contain concentric and radial euhedral calcite fillings within a micro-brecciated, cryptocrystalline, micro-sparitic or feathery to variolitic carbonatic matrix. In addition, yellowish to orange carbonate concretions with irregular shapes and with cryptocrystalline to micro-sparitic carbonatic matrix occur.

3.2.2 Carbonate and manganese spheres

Isolated spheres between < 1 mm to several mm are found after washing large samples of unconsolidated clastic material in the south wall of the larger westerly lake as well as in the material of the excavated trench. Their grain size comprises a few millimeter. The concentric, spheroidal shapes as well as the internal aggregate micro fabrics indicate that they formed by accretion of small solid particles. One variety has concentric layers of crypto- to microcrystalline aggregates of iron and manganese oxides alternating with carbonate and clay-rich layers. These spheres resemble at first glance small common manganese nodules. However, they are throughout spattered with polymict fragments, mainly quartz and cherts; similar to the majority of all brecciated clasts, and thus, may have been formed by a totally different geological process. In addition, the spheres contain xenomorphic inclusions of rutile, zircon, monazite and spinels. A second variety of spheres consist of silicate/carbonate micro-brecciated groundmass, in some cases with "porcelain-type" cryptocrystalline matrix.

3.2.3 Calcite and quartz spheroidal particles

Two examples of individual spheroidal particles are shown in Fig. 6a and b, e.g. a carbonate-silicate sphere with concentric rims and microcrystalline silicate core in a feathery calcite matrix. A variety of fine-grained lithic breccias and clasts are made up of "carbonate spheroidal particles" with dimensions between 0.1 to 1 mm, which occur either as individual spheroidal particles or exhibit coalescent bounding (Fig. 4e). Some spheroidal particles, which are made up of cryptocrystalline, "porcelain-type" to

SED
5, 1511–1573, 2013

microcrystalline carbonates. Ideally shaped spheroidal particles "spherules" containing feathery, arborescent and even variolitic calcite crystallites have not been observed.

Another characteristic variety of spheroidal clasts, which occurs in small quantities and dimensions from µm to cm with black glassy appearance, consists of cryptocrystalline to microcrystalline quartz or spheroidal particles (Fig. 4i), made up by fine radial quartz fibers. The white, interstitial matrix consists of cryptocrystalline and feathery quartz; the black parallel micro-fractures are filled with iron- and manganese oxides. These spherulitic quartz clasts as well as other pure quartz fragments are spotted with small euhedral calcite crystals and minuscule 5–10 µm sized inclusions and globules of cryptocrystalline calcite aggregates (Fig. 6h and i), spinel, apatite and not yet properly identified iron oxides and sulfides, containing silicon, barium, calcium, phosphorous, and fluorine.

Many breccias contain "spheroidal shaped particles" with dimensions between 0.1 to 1 mm (Figs. 4f). They are composed of micrometer-sized micro-sparitic low-Mg calcite and contain small amounts of sulfur. Often they inhibit fragmental nuclei of quartz, cherts, and feathery to arborescent carbonate fragments. In most cases the fragments are mantled with rims and coronas of submicroscopic carbonate and clay mineral assemblages (Figs. 8b and d). These spheres are neither "secondary vesicle fillings" nor "ooid-like, ideal-shaped concentric layers" of perpendicular crystallized calcite aggregates, but they are made up of irregular distributed cryptocrystalline to microcrystalline and fine-grained euhedral carbonates with "schlieren" and feathery to arborescent textures. The interstitial matrix between the spheres is made up of fine- to coarse-grained euhedral calcite crystals.

3.3 Feathery calcite matrix of breccias and clasts

Calcite is the major constituent of the carbonate matrix in most of the Zerelia clasts, spheres and spheroidal particles. It occurs as sub-microscopic to microscopic feathery, arborescent and variolitic aggregates (Fig. 4a–d) as well as cryptocrystalline to micro-

SED
5, 1511–1573, 2013

sparitic and euhedral grains. In addition, large xenomorphic crystals often with mosaic textures exist as fillings of calcite veins.

Feathery calcite (FC) occurs as fine-feathery crystallites in the inner parts of the spheres and progressively become coarser towards the outer parts (Fig. 4a). In all cases, the feathery calcite aggregates are spotted with tiny quartz fragments (Fig. 4b and c) throughout the entire clasts and spheres. Inside larger spheroidal, "septarian-type" clasts fine feathery calcite has crystallized as first generation within the outer zones of radial and concentric calcite veins.

In general, it is pure calcite, in some cases, such as in feathery aggregates, it is silica, alumina and magnesia bearing due to a submicroscopic intergrowth with quartz and clay minerals; within zoned veins manganese-calcite appears. Of particular interest are the compositions, different generations of feathery calcite crystals, groundmass matrices of spheres and spheroidal particles, "glass-shaped" illite-kaolinite fragments, and calcite veins.

3.4 Recrystallized "fluidal and curved glass fragments"

Several carbonatic clasts with feathery textured calcite groundmass contain recrystallized "fluidal and curved glass fragments" dense reddish and brownish submicroscopic patches of clay aggregates (Figs. 4g and h, 6d and e), which according to X-ray powder diffraction, consist of mixtures of illite and sericite, kaolinite and goethite. Their characteristic chemical composition in wt.% is: SiO_2 = 50–52, Al_2O_3 = 20–32, K_2O = 2.0–2.8, SO_3 up to 1.3, but low in CaO = 2.6–2.8, NiO up to 0.2 and Cr_2O_3 up to 0.1. These fragments of different size and shapes are embedded within feathery calcite aggregates and crosscut by a fine network of granular calcite, which does not extends into the feathery matrix.

Most of these compositions may represent mixtures of cryptocrystalline mineral phases, and do not match at all any known bulk chemical composition of altered and recrystallized volcanic glass. All values do not represent analytical problems, since similar features have been analyzed also in other impact carbonates (Osinski et al., 2005).

SED
5, 1511–1573, 2013

It could be shown that high-temperature quenching of SiO_2-bearing calcium carbonate melt can produce SiO_2-rich carbonates (Brooker, 1998; Brooker and Kjarsgaard, 2010).

3.5 Calcite crystallization sequence (veining)

The relative sequence of calcite crystallization sequence in the ejecta is clearly expressed by veining textures. However, veining is absent in dense lithified polymict breccias type A and B, shown in Fig. 3c and d. Calcite veining is a common feature in most carbonate clasts and occurs in all sizes from spheroidal particles, to clasts of several centimeters (Fig. 5b). Euhedral calcite in different textural arrangements is the predominant vein-filling phase; magnesia and iron bearing calcite and dolomite are subordinate.

Two different sets of veins can be distinguished within the polymict breccias and clasts: (A) veins, which are mainly filled by feathery and euhedral quartz crystals with subordinate growth of idiomorphic and irregular small patches of calcite. Such veins are restricted to polymict type B breccias and clasts with spherulitic and micro-sparitic textures; one typical example is given in Fig. 5b. The sequence of crystallization is numbered with 1, 2, and 3. Magnesium and iron bearing calcite assemblages with microcrystalline and partly feathery textures represent the first crystallization stages (No. 1) and are often associated with iron and manganese oxides (e.g. with psilomelane). Coarse-grained euhedral calcite crystals mark the later stages filling the inner parts of the veins; (B) a disseminated vein network of micro-sparitic to euhedral calcite, which penetrates the entire clast (e.g. Fig. 4g and h). Exceptions are radial and concentric veins as well as cavity fillings in spheroidal "septarian" shaped clasts.

3.6 Quartz and chert aggregates

Quartz is the second most common mineral in the breccias of the walls around the lakes. It occurs in the polymict breccias as fragments of Jurassic radiolarian cherts,

SED
5, 1511–1573, 2013

recrystallized cherts in all dimensions and deformational states from micron to centimeters sizes. At present, only the low p/T modification α-quartz has been found up to now using X-ray diffraction and in a few ~~RAMAN~~ spectra. However, one ~~RAMAN~~ spectra showed the characteristics of weakly crystallized silica glass similar to spectra from diaplectic glass found in lithic lasts from the Ries impact crater (Stähle et al., 2008). The deformational features in quartz fragment will be shown in a later paragraph are shown in Fig. 5a–f.

The majority of quartz fragments within clasts of feathery calcite aggregates and in cryptocrystalline "porcelain-type" carbonate matrices of spheres and spheroidal particles exhibit angular to subrounded shapes: µm-sized grains with sharp rims, the larger grains with calcite reaction coronas. In the spherulitic breccias with micro-sparitic to sparitic fabrics, quartz appears with sharp or slightly frayed rims, partly with bulged and with cryptocrystalline to micro-sparitic calcite coronas. ~~Often~~ quartz fragments are spotted with minuscule calcite globules and other mineral inclusions (Sects. 3.6 and 3.7, Fig. 6f–i). Micro- and cryptocrystalline quartz aggregates (chert and radiolarian chert, spherulitic aggregates) with local quartzine and chalcedonic quartz are also present. Mottled chert clasts and fragments consist of micro- and cryptocrystalline quartz, length-slow chalcedonic quartz and mosaics or individual crystals of euhedral quartz.

3.6.1 Deformation in quartz

Small fragmental quartz grains of up to 100 µm are very abundant in the Zerelia breccias, clasts, spheres and spheroidal particles. ~~Often the~~ fragments show undulate extinction and Boehm lamellae. Many quartz fragments are internally fractured (e.g. Fig. 5a) and show mosaic (Fig. 5b) and "moertel" textures. In addition, brittle deformation ~~occurs~~ in larger quartz fragments decomposed by a network of calcite veins (Fig. 5b). In some fragments subplanar and subparallel deformation lamellae (Fig. 6a) as well as weak "planar fractures ~~(PFs)~~" are present (Fig. 6b and c). A ~~perpendicular~~ fractured quartz fragment in a patchy feathery calcite matrix with calcite reaction rim

SED
5, 1511–1573, 2013

is shown in Fig. 5f. Several small internally curved fractures indicate the existence of former gas bubbles (sample Sph11).

3.6.2 Chemical composition of quartz

In general, most of the analyzed quartz fragments turned out to be pure SiO_2. In some cases, small fragments inherit irregular patchy distribution of alumina between 3 and 4.5 wt.% Al_2O_3. The analysis does not permit to answer weather alumina is replacing silicon or it occurs as a separate phase of alumina oxide. A few quartz fragments (e.g. in sample AlmX and G, see Fig. 6a and f, respectively) show remarkable unusual high amounts of iron up to 2.3 wt.% FeO and nickel up to 0.59 wt.% NiO.

3.7 Globules and exotic mineral inclusions in quartz fragments

Numerous quartz fragments contain in random number and distribution globules up to several µm in size. In several cases they consist of calcite (Fig. 6h and i) and subordinated dolomite, which will be discussed later. In addition, µm-sized exotic globular and irregular, partly skeletal shaped inclusions in quartz have been detected.

They represent improperly identified (Mg,Ca)(Al,Si) Fe-phases and (Mg)(Al,Si) Ti-Fe-phases containing alumina, silica and sulfur bearing Fe-phases or oxides or (e.g. Fig. 6g). Some of them contain nickel (NiO = 0.1–0.6 wt.%). It is difficult to establish their mineralogical character without precise microprobe analyses due to their size. They could represent solid solution phases or mixtures of quartz, alumina, iron-titanium oxides and elemental iron.

3.8 Fragments of accessory minerals: ilmenite, rutile, spinel and zircon

The accessory mineral phases ilmenite $FeTiO_3$, mangan-ilmenite, rutile TiO_2, magnetite, Fe_3O_4, titano-magnetite, Mg-Al-Fe chromspinel, zircon $ZrSiO_2$, monazite $CePO_4$ and xenotime YPO_4 occur in the shape of xenomorph micro-particles as xenomorph fragmental inclusions in the carbonatic polymict breccia, clasts, spheres,

SED
5, 1511–1573, 2013

and spheroidal particles as well as inclusions in quartz fragments as well as between feathery, arborescent and variolitic calcite matrices (Fig. 7a–f). Also apatite $Ca_5(PO_4)_3F$, and not yet defined (Mg,Ca)(Al,Si) Fe-phases as well as relics of antigorite, micas and feldspars have been found as small inclusions in quartz fragments (Fig. 6f). In addition, minuscule inclusions within quartz fragments and interstices between feathery calcite aggregates turned out to be not yet properly defined compositions of Ti, Al, Si bearing iron-rich phases. X-ray Powder Diffraction on decarbonated breccias showed the ambiguous existence of periclase (MgO) and millerite (NiS).

While the tiny, even < 1 µm inclusions exhibit skeletal textures (e.g. rutile and ilmenite), the larger fragments, generally > 10 µm sized, are bulged with irregular shapes and hollows. In some cases, small zircon crystals exhibit blurred "granular" textures (Corfu et al., 2003; Tohver et al., 2012) and contain domains of irregular composition, rich in uranium, thorium and other elements as shown in Fig. 7d–f.

3.9 Iron- and manganese oxides

Late impregnations of dendritic iron- and manganese oxides occur mainly on the surface of the clasts. Often the outermost surface of small spheres consists entirely of these oxides (e.g. Fig. 4d and i). Along hairline cracks they can enter innermost parts of the clasts and precipitate in empty spaces and pores (Fig. 4i). Minor minerals species include dolomite, iron and manganese oxides and aggregate mixtures with silicates: goethite FeOOH and boehmite MnOOH, manganocalcite $(Ca,Mn)CO_3$. The textures of such cryptocrystalline aggregates suggest a very late state of formation under subsurface and surface atmospheric conditions.

4 Bulk rock chemistry breccias and clasts

The XRF bulk rock chemical composition of 15 representative samples of the unusual carbonate clasts, breccias and subsurface grab samples is given to demonstrate their

SED
5, 1511–1573, 2013

chemical characteristics (Tables 1 and 2). The goal is the distinction from Neogene and Mesozoic bedrock formations. Two fossiliferous limestone samples M and E out of the unconsolidated sediments from walls around the smaller lake ZLE (Table 1) for comparison are chosen, which seem to be only slightly altered since they contained only a very fine network of calcite veins decorated with iron and manganese oxides.

The bulk chemical composition of the larger spheres and clasts (see Sect. 3.2) cannot be compared with the chemical composition of the micro-crystallites and mixtures of minerals with the EDX spot analyses of 1 µm and less. The latter are mineral composition whereas the XRF analyses (Table 1) represent bulk compositions of the polymict breccias. Five samples, AS1, F22 and Alm16, Alm17 and Alm18 are orange colored dense spheroidal clasts of 3–5 cm in diameter with cryptocrystalline, micro-sparitic to feathery calcite groundmass, one dense white-yellowish altered clast (D11). The four samples ZLE1, ZLE2 and ZLW1, ZLW2 (Table 2) represent 10 g aliquods from approx. 1 kg washed and coarse to fine sand grab-samples of the subsurface unconsolidated breccia material from the eastern wall of the smaller lake ZLE and from southern sampling outcrop (SP1 in Fig. 1) of the larger lake ZLW. The samples ZLWD1 and ZLWD2 represent ca. 20 g aliquods of 30 cm long and 5 cm diameter drill cores into the lower unconsolidated wall of the southern outcrop SP2 and from the clay rich creek wall at the northern spill of lake ZLW, SP2. The three samples ZLWS represent a silt, a decarbonated silt, and a clay fraction of the grab sample ZLW1. The amounts of quartz and chert fragments and disseminated cryptocrystalline smectite are estimated in vol.% according to thin sections: AS1, F22, and Alm16, Alm17 and Alm18 = 1–3; D11 = 5–10. In addition, all clasts have Fe-Mn-oxides impregnation in their rims.

The major elements of the clasts show a rather marly limestone composition, demonstrated by analyses of the two clasts D11 and F22 in Table 1: with SiO_2 = 30–34 wt.%, CaO = 28–32 wt.%, Al_2O_3 = 5–5.7 wt.%, K_2O = 0.6–0.75 wt.%, TiO_2 = 0.35–0.45 wt.%, Fe_2O_{3tot} = 2.1 w.t%, and MgO = 0.65–0.9 wt.%: the other clast analyses are similar in their major composition depending on the amount of polymict fragments. The variations in trace element contents are: Rb 51–62 ppm, Sr 60–103 ppm, Ba 228–678 ppm,

SED
5, 1511–1573, 2013

Nb 10–15 ppm, Light Rare Earth Elements (Ce 48–108 ppm and La 59–102 ppm); Cr 174–252 ppm, Ni 86–108 ppm and Zn 43–63 ppm. The only unusual enrichment exists in Y with 36–96 ppm and Zr 145–147 ppm.

The sand, silt and clay fractions of unconsolidated grab and drill samples (Table 2) show generally much higher contents ~~of~~ Al_2O_3 = 8.2–15.9 wt.%, K_2O = 0.9–1.9 wt.%, MgO = 1–3.4 wt.%, Fe_2O_{3tot} = 3.9–7 wt.% and Rb = 40–110 ppm, which can be explained with the high amounts of clay minerals and iron oxides in the unconsolidated material., In addition, higher values occur for yttrium, the rare earth elements as well as for nickel and chromium (Ni = 83–185 ppm and Cr = 176–294 ppm). Exceptional high values of sulfur (4630 ppm in ZLE-1) and strontium (1472 ppm in ZLWD-1 total silt) are present in two samples. ~~Interesting is the fact that~~ the fine grained clay-rich drill sample ZLWD2 (Table 1) as well as the clay fraction ZLWS1 (Table 2) contain similar amounts of zirconium, nickel and chromium, which is probably due to µm-sized particles of zircon, spinels and possibly iron-nickel bearing nodules.

All carbonate clasts, the drill and grab samples have similar bulk chemical characteristics, in terms of magnitudes for major and trace elements disregarding Si, Al, Fe, Mn, and K, which reflects the contamination of the fragmental quartz, cherts, clay minerals, goethite and Fe-Mn-oxides. Remarkable is the rather low composition of Mg, which might be explained by the absence of dolomite~~s~~ and basic to ultrabasic rocks (ophiolitic components) in the bedrock formations. The clasts are ~~obviously~~ enriched Ti as well in the amounts of P, S, Cl, and F compared to the composition of the two selected limestones M and E. Similar enrichment can be recognized in the polymict breccias for Ba, Rb, the light rare earth elements (LREE), for all transitional elements Cr, Ni, Co, Zn, Cu, V as well as in Nb, Y and Zr.

The presence of P, F, Ba and LREE can be explained with their occurrence of phosphorite and Mn-minerals in the manganese deposits of the radiolarian cherts in the bedrock formations. Chlorine ~~obviously~~ is present in the lacustrine shales of the Neogene sediments. Ba and parts of the transitional elements as well as Y and Zr are

SED
5, 1511–1573, 2013

bound in the heavy minerals apatite, rutile, ilmenite, magnetite, spinel, monazite, and xenotime.

5 Geophysical investigations

5.1 Gravity measurements and modeling

A gravity survey was carried out in the area of the Magoula Zerelia twin lakes to establish the Gravity Anomaly Field. About 80 gravity measurements were taken by the use of the LaCoste and Romberg G-496 gravity meter. The gravity measurements were irregularly taken at a spacing of about 100–150 m at an effort to cover satisfactorily all area around the two lakes. The nearby pillar (No. 109086) of the Hellenic Military Geographical Service at the hill between the two lakes (Fig. 1) provided the coordinates, not only in the vertical, but also in the horizontal., A geodetic dual frequency GPS receiver of LEICA (type AX1202) was mounted on top of the pillar recording every 5 s, and served as a base station (particularly for the vertical component) for the kinematic GPS survey for the coordinate determination of the gravity stations. The rover GPS station was of the LEICA type SR299, which was recording for a period of 3–4 min at every gravity station to determine basically the height with an accuracy of better than 1–2 cm, even though the accuracy in the horizontal coordinates was much higher (< 1 cm). A gravity base station was established nearby the HMS pillar, where repeat measurements were performed every 3–4 h for control of the gravity meter drift. The field gravity base station was tied up to the Athens University IGSN'71 absolute value gravity station (Hipkin et al., 1988). The gravity measurements were reduced to gravity anomaly values, where terrain corrections were performed at a distance of about 22 km around each station. Therefore, all gravity values of the gravity survey are based on the Gravity Reference Formula of 1967 (GRF'67) and referred to IGSN'71.

It was found that a surface density of about 2.10 (±0.20) g cm^{-3} was appropriate to reduce the gravity anomaly values after fitting a 3rd degree polynomial to the observed

SED
5, 1511–1573, 2013

gravity anomaly field (Hipkin and Lagios, 1980), instead of reducing the gravity measurements with the conventional standard Bouguer density of 2.67 g cm^{-3}. This applied procedure allows the determination of the true amplitudes of the gravity anomalies that would subsequently result in the proper and actual amplitudes of the residual anomalies to be modeled after the subtraction of the regional gravity trend.

The reduced Gravity Anomaly Map (Fig. 8) shows two gravity lows associated with the localities of the two lakes, reaching values of about 115 and 125 gravity units (gu). However, for the modeling procedure, the Residual Gravity Anomaly Map (Fig. 9) was formed. It was calculated that a linear regional trend of about 5 gu/100 m should have been subtracted from North to South for the compilation of the residual gravity anomaly map. The regional gravity anomaly map of the broader area (Lagios et al., 1995, 1996) was also taken into consideration for the estimation of the regional trend to be subtracted from the gravity anomaly map of Fig. 8. Both maps (Figs. 8 and 9) are overlain by the Google earth image of the area, where the two lakes may easily be seen.

The analysis of the gravity anomaly map showed that the resultant residual gravity anomalies are about 10 gu and 17 gu associated with the eastern and western lake, respectively (Fig. 10). The western larger lake is characterized by also a larger residual anomaly encompassing almost all of the ground depression extended beyond the banks of the lake, and with an offset of the residual low to the west from the center of the lake. Another gravity low but of smaller amplitude is also formed at the NW margins of the map. The gravity low associated with the smaller lake on the East fits within the lake diameter, however slightly elongated to the North, where another low is also formed, but of lower anomaly amplitude (≈ -5 gu). It has to be noticed that all gravity contours overlain the two lakes are interpolated artifacts, since there was no possibility to perform gravity measurements in the two lakes. Therefore the almost linear contour shape observed at their NE margins should rather be attributed to the interpolation effect, showing a deviation from the circular pattern.

SED
5, 1511–1573, 2013

5.2 Gravity anomalies of impact structures

Gravity anomalies in impact structures may result from ~~quite~~ different processes. Small, simple craters in general show a roughly circular negative anomaly, as actually happens in our case in this study. The mass deficit could be due to low-density sediments (such as breccias) of young lake sediments and unconsolidated debris underneath the present day floor as well as fracturing of the bedrocks beneath and around the lakes.

Two profiles (Profiles 1 and 2) of W–E direction were drawn for modeling (Fig. 9). A single interface with a density contrast of $-350\,\mathrm{kg\,m^{-3}}$ was applied between the basement and the ~~overlain~~ sediments. Modeled depths of 180 m and 260 m were resulted for the eastern and western residual anomalies (Fig. 10). It has to be noticed that the dimension of the "modeled crater size" is larger than the size of the lake diameter, consistent with the present morphology and topography of the region. Pilkington and Grieve (1992) have considered theoretical curves between amplitude of gravity anomalies (Δg) produced by various impacts and their associated crater dimensions. Considering the "model crater dimensions" of the eastern (240 m) and western (450 m) lake, values of about 11 gu and 20 gu are resulting from the empirical curve (Δg vs. Crater Model) for the estimated density contrast of $350\,\mathrm{kg\,m^{-3}}$. These values constitute a discrepancy of 10 % and 15 %, respectively, meaning that the adopted density contrast appears to be over-estimated by 10–15 %. Comparing also the "modeled crater" diameter (240 m and 450 m) with the depth to model base (Pilkington and Grieve, 1992), values of 170 m and 300 m are theoretically produced; therefore, when compared to 180 m and 260 m model depths (Fig. 10), the discrepancy ranges between 6 % and 13 % for the eastern and western lake, respectively. It therefore appears that our model parameters are within acceptable limits, even though a single interface was used in the gravity modeling.

The form and shapes of the residual negative gravity anomalies of the Zerelia twin-lakes are consistent with those in other areas of the world, where meteorite impacts occurred, as the Steinheim impact (Ernstson, 1984; Therriault et al., 2002). The mod-

SED
5, 1511–1573, 2013

eled negative gravity anomalies through both lakes appear to indicate a structure close to a bowl-type form of a crater, taking into account the inherent interpolation artifacts associated with the linearities at some parts of the anomalies over the lakes.

In general, the negative gravity/density anomalies underneath both lakes are the result of a combination of unconsolidat[ed] mud, a mixture of clay rich detrital sediments in the upper part and a ~~highly shattered~~ brecciated zone of debris fillings (such as quenched carbonate [bre]cias) in the lower part. These features are supported by the differences of the ~~ejected~~ brecciated material. The asymmetric flanks of the western lake contain a large amount and variation of polymict carbonate breccias whereas the walls of the eastern lake are made up of a limited variety of breccias, clasts, transformed carbonates and limestones.

Two profiles (Profiles 1 and 2) of W–E direction were drawn for modeling (Fig. 10).

5.3 Magnetic measurements

Total field magnetic measurements were conducted in the same gravity survey area to determine the Total Magnetic Field at an effort to detect magnetic anomalies relating to the probable presence of a magnetic body supporting the suggested meteorite impact hypothesis. More than 400 total field magnetic readings were performed using total field magnetometers of the GEOMETRICS G-856 type along 12 profiles and peripherally around the two lakes at a spacing of 10 m. During this time a separate magnetometer was continuously recording at a nearby site every 1 s to form the daily variation of the local magnetic field. The coordinates at each station were determined by the use of a Magellan GPS receiver with an accuracy of better than 2–3 m. Corrections for the normal field and the diurnal variation were made to calculate the magnetic anomaly value for each station.

A Total Field Magnetic Anomaly map was thus constructed from all stations (Fig. 11). It appears that the magnetic field north of both lakes has positive values (exceeding the amplitude of 100 nT at the western part), which generally showed positive anomalies, and should be attributed to the spatial distribution of the basement rock formations.

SED
5, 1511–1573, 2013

Another positive feature is also associated with the hill separating the two lakes, which is build up by the remains of Neolithic settlements.

The two lakes are associated with two low magnetic anomaly patterns. The eastern lake is dominated by a relatively large negative magnetic anomaly (−100 nT) encompassing even a region outside the lake, west and south, as well as a positive anomaly at its eastern flank that may be attributed to the approximate 50 nT anomaly basement characteristic. The situation on the western lake is almost the same; a negative anomaly dominates its southern flank, which swings also to the west along its western part. However, the northern flank of the lake is associated by positive anomaly values. Since no readings have been taken on the surface of both lakes, the magnetic anomaly values that have been deduc[illegible]y interpolation have been blanked over their surfaces.

The dominant effect over craters is a magnetic low ranging in amplitude from tens to a few hundred nT (Clark, 1983). This type of signature is most easily recognized and should rather be attributed to the truncation and disruption of regional basement magnetic trends. The magnetic lows are best defined over simple craters, where the anomaly is smooth and simple, while normally a broad correlation exists between anomaly form and crater size: structures with crater diameters less than 10 km all are associated with magnetic lows (Pilkington and Grieve, 1992), as actually happens in the present study.

Therefore, the magnetic anomaly map should only qualitatively ~~be considered~~. However, the higher magnetic values in the marginal walls of both lakes correspond to higher susceptibility values of the brecciated surface material and are consistent with the appearance of magnetite grains as relics from serpentinite rock from the bedrock. The amount of serpentinite with magnetite found in all clasts, breccias, and spheroidal particles, is very small not exceeding a few per mille.

SED
5, 1511–1573, 2013

6 Discussion

6.1 The contrasting hypothetical origin of the enigmatic Zerelia twin-lakes

Several hypotheses could be drawn upon to explain the origin of the twin-lakes: (a) Maar-type volcanic craters; (b) hydrothermal or CO_2/hydrocarbon gas explosion craters *producing "mud volcanoes"*; (c) and (d) doline holes due to karstification; may-be in combination with pre-historic "shepherdogenic" activity; or (e) ~~unusual~~ small meteorite impact craters.

6.1.1 Origin due to a Maar-type, diatreme, volcanic explosion

A hypothesis as volcanic maar-type diatremes has been suggested on the basis of the existence of small Pliocene trachyandesitic volcanic centers in the wider area (Marinou, 1963; Marinos and Papakis, 1965; Innocenti et al., 1979). Although small volcanic tuff pipes occur worldwide in intra-plate volcanic-fields, even erupting carbonatitic magma from deep mantle depth (e.g. the Italian Polino diatremes in Umbria, Stoppa and Lupini, 1993), a comparison with the Zerelia lakes cannot be made. No other volcanic or volcano-clastic material with relict mantle inclusions has been detected in the entire brecciated material around the Magoula Zerelia lakes. In addition, the chaotic unconsolidated clastic sediments in the two outcrops of in the relict walls of the larger lake ZLW (Fig. 1) and in the excavated trench do not show signs of sorting and stratification (Fig. 3e). Diatreme/maar producing volcanic explosions usually continue in multiple phases for hours and days, and therefore produce typical maar-type tuff-layering structures.

However, the existence of the polymict breccia containing strange quenched feathery calcite could lead to an interpretation of a volcanic eruption of carbonatitic magma. The quenched textures of calciocarbonatite melts and lavas also resemble very much those of the Zerelia carbonates. Carbonatitic extrusives are very rare and occur in alkaline volcanic fields (e.g. Keller, 1981; Hoernle et al., 2002; Mourão et al., 2010) or

SED
5, 1511–1573, 2013

in kimberlite pipes. In addition, the bulk chemical composition of the Zerelia breccias does not match those of magmatic carbonatites.

6.1.2 Origin due to a hydrothermal and hydroclastic explosion

In general, such explosion craters are formed only in active volcanic fields with strong hydrothermal activity in the bedrock due to long lasting hydrothermal systems linked to large plutonic bodies and multiple magma input (e.g. in the Neogene Aegean volcanic arc islands, Milos, Santorini and Nisyros). The whole Almiros plain and the entire neighborhood of Magoula Zerelia do not show signs of hydrothermal activity, present and past. The brecciated material, occurring in the walls and slopes around the lakes, distinctly differ from hydrothermal deposits. Subsurface and surface boiling processes would have produced travertine deposits and veining with characteristic depositional textures. However, such a possible origin cannot be totally excluded.

6.1.3 Origin due to a CO_2/hydrocarbon gas explosion producing "mud volcanoes"

Mud volcanoes are mostly found in areas of high volcanic activity or places with oil and natural gas depositions. They are a result of the increase in tectonic activity or a pressure build-up under the surface. An earthquake may affect a CO_2/hydrocarbon gas reservoir under pressure, leading to an explosion and forming a "hole-type mud volcano". Classical examples exist in many parts of the world, e.g. Azerbaijan and Trinidad (Hosein, 2006). Such an interpretation has also been issued the "Sirente crater" by Stoppa (2006), mentioned above with another hypothesis. An origin of a "single event mud volcano explosion" for the generation of two explosion holes of similar dimensions next to each other can be excluded due to the unique breccia-like material in the embankment of the lakes, to the partial melted high-temperature resistant minerals, and to the absence of any gas/hydrocarbon emissions or similar activity in the entire area.

SED
5, 1511–1573, 2013

6.1.4 Origin as dolines by karst formation

Circular lakes and steep holes of similar dimensions occur in many areas throughout Greece within karst environments and limestone formations of different geological ages. Typical doline lakes are distributed in the area between Vonitsa and Lefkada (western Greece, Ionian islands). All the doline holes and lakes within these Mesozoic limestone formations have no elevated outside walls, their inside walls are steep to vertical and show neither alteration nor fracturing and brecciation; the water-depth varies seasonally dramatically. If classical doline holes are filled, the material reflects mainly the surface material of their neighborhood. In the case of the Zerelia lakes typical detrital Mesozoic and Neogene limestones and marls are missing.

In contrast, besides the two Zerelia lakes no other similar circular holes exist in the vicinity, in the entire Almiros plain, and in the Othris foothills. No tectonic structures, such as faults and scarps have been found around the lakes or are apparent on satellite images. With the exception of two small springs no natural water sources are present in the neighborhood of the lakes. According to an old story by Theocharis "the temple of Athena Itona is situated in one of the two lakes and only visible when the lake falls dry", which only happened in 1980 after an earthquake (Reinders, 2004). The only explanation of this phenomenon is that their bottom is filled with clays, marls and debris breccias within a bowl shape structure, which prevents drainage of water.

Gravimetric modeling supports such a bowl structure (see chapter 6, Geophysical investigations). The larger Lake ZLW has only a morphological depression with a small stream at the southern rim and a small spill and creek at the northeastern rim (Fig. 1), controlling an overflow during seasonal flooding due to heavy rain and thunderstorms.

However, karst phenomena including small bauxite deposits as fracture fillings exist in the Mesozoic limestone formations of the bedrock of the wider area (geological maps of Greece 1 : 50 000: sheet Anavra, Marinos et al., 1957 and sheet Almiros, Marinos et al., 1962). In several places of the Almiros plain poorly cemented "Red Bed type" clastic matrix-supported sediments unconformably overlay alluvial Pleistocene marls

SED
5, 1511–1573, 2013

and sandstones, probably representing arid climatic conditions. Therefore, an origin of the lakes as a karst phenomenon cannot be entirely excluded.

6.1.5 Origin as combination of a natural "karst depression" with "shepherdogenic" activity

A comparable ~~similar~~ shallow ~~lake~~ in size is located at the center of the Prati del Sirente, a mountainous highland north of the Sirente massif in the Apennines (central Italy), has been postulated as a "meteorite crater lake" by Ormö et al., (2002, 2006, 2007). In contrast, a shepherdogenic origin (human excavation for collecting water for livestock) was proposed for the lake Sirente by Speranza et al. (2004) based on geoelectric profiling and the lack of typical impact ejecta in the crater walls.

Such an origin ~~can be excluded~~ due to the more than 20 m prehistoric depth of the lakes (Reinders and Bottema, 1983) as well as to the gravimetric results.

7 The origin of the Zerelia twin-lakes by a possible meteorite impact

Up to now, 180 individual morphological and geological structures have been identified as ~~preserved impact craters~~ worldwide (compilations and extensive documentations: French, 1998; Kenkmann et al., 2005; Osinski et al., 2008; Evans et al., 2008; Gibson and Reimold, 2010; and in the "Earth Impact Database", 2013). The known impact craters range from small circular bowls (partially as lakes) only a few kilometers or less in diameter to large complex structures more than 200 km in diameter and as old as 2 Billion years. Only ~~37~~ craters exist in Europe, mainly in geological old crystalline basement rocks in Fennoscandia and Ukraine, only 2 in southern Germany and 1 in France, none in the entire Mediterranean.

Impact craters, similar in size and Holocene age to the Zerelia lakes exist in Estonia (e.g. the Kaali craters in the island of Saarema, Veski et al., 2001, 2004; Raukas et al., 2005; ~~and the Ilumetsa crater, Henkel and Personen, 1992~~; Raukas et al., 2001) as well

SED
5, 1511–1573, 2013

as in the Neolithic Morasko crater field in northern Poland (Stankowski et al., 2002, 2006). ~~According to magnetic and seismic reflection studies, a small lake of similar dimensions, "Lake Cheko" in Siberia, has been estimated as possible impact crater due to the mysterious large Tunguska asteroid blast 1908 (Gasperini et al., 2008, 2012).~~

The hypothesis of the origin of the Zerelia twin-lakes due to meteorite impact is based on the finding an unusual high amount of angular clasts and pebbles of dense polymict lithic breccias in the sandy-silty clay only along their shores and their proximal vicinity during reconnaissance investigations 2008 and 2009 (Dietrich and Gartzos, 2009), which did not resemble to any of the common limestone detritus in the neighboring agricultural fields. Many brecciated carbonate fragments as well as carbonate lapilli showed distinct microscopic features of melting and recrystallization, e.g. feathery calcite textures. Very similar feathery calcite aggregates were reported from ejecta of several meteorite craters and interpreted as ~~quenched results from~~ carbonate melts (see compilation in Osinski et al., 2008, 2011): e.g. in immiscibility blobs in suevites of the ~~14~~ Ma Nördlinger Ries Germany (Shoemaker and Chao, 1961; Graup, 1999; Reimold et al., 2012); Steinheim crater Germany (Anders et al., 2011); in accretionary lapilli from the ~~65~~ Ma Chicxulub Crater Mexico (Alvarez et al., 1980, 1995; Schulte et al., 2009); in fragments and spherules of the late Devonian ~ 382 Ma Alamo event (Pinto and Warme, 2008); in fragments in the 35 Ma Chesapeake Bay impact structure (Vanko, 2009).

7.1 Recognition of shock-metamorphic effects ~~during a meteorite impact~~

The detection of shock metamorphic effects in rocks and minerals can be used as a powerful tool to confirm and study impact structures and the associated effects of impact-induced melting. This applies to crystalline as well as for sedimentary-hosted impact craters. Reviews are given by French (1998), Bischoff et al. (2006), Osinski (2007), Osinski et al. (2008, 2011), Stähle et al. (2008), Trepmann (2008), French and Koeberl (2010), Gibson and Reimold (2010), and Reimold et al. (2012). The kind of shock-metamorphic effects (fracturing, brecciation by brittle deformation, melting and

SED
5, 1511–1573, 2013

recrystallization) depend highly on the physical conditions, pressure and temperature generated during the impact, which are related to the size and type of the meteorite and its impact angle and velocity. Only low impact pressures below < 10 GPa might be estimated for the rather small dimensions of the Mougulia Zerelia twin-lakes due a meteorite impact based on the observed textural phenomena in the clasts and minerals of the polymict breccias. Very similar criteria in polymict breccias designated as "back-fall ejecta" have been described from several impact craters by (Langenhorst et al., 2000; Osinski et al., 2005, 2008, 2011; Schulte et al., 2006; Yancey et al., 2008).

Several characteristic deformational features, which are interpreted as shock-metamorphic effects, can be distinguished in the breccias from the Zerelia lakes. This implies in particular to the brecciated material around the larger lake ZLW. No traces of shatter cones have been recognized in the larger breccia blocs.

7.1.1 Fracturing and brecciation

In thin sections, mainly quartz and feldspar as well as chert and subordinate schist fragments, which are frequently angular with sharp edges indicate that they are broken clasts derived from the Mesozoic and Neogene bedrock formations by instant fracturing. Quartz fragments range in size from a few µm to mm and often show deformational effects ranging from simple fracturing through brecciation up to entire disintegration (Fig. 5a and b). In contrast, the majority of chert fragments show only fracturing and partly a weak deformation.

7.1.2 Quartz and calcite deformation

Often quartz fragments show undulate extinction and Boehm lamellae, which may be results of tectonic and metamorphic deformation in the crust during orogenic processes. However, subplanar and subparallel deformation lamellae (Fig. 5c) as well as weak "planar fractures (PFs)" are present (Fig. 5d and e) in some quartz fragments, which might be interpreted as a result of low-pressure shock-metamorphic effects. Sim-

SED
5, 1511–1573, 2013

ilar PFs have been described from meteorite impact craters of similar sizes and ages, the Aouellloul crater in Mauretania (Koeberl et al., 1998) and the Macha crater in Yakutia (Gurov and Gurova, 1998; Hamers and Drury, 2011). Sharp, straight, parallel "planar deformation features (PDFs)" have not been detected in the examined material.

Apparently, calcite deformational effects can be produced in target limestones by impact shock metamorphism (e.g. Burt et al., 2005 in the Arizona Barringer crater).

High-density planar calcite twins and offset small loops of twins and cleavages are present in partly preserved larger shell fragments in some limestone clasts with weakly recrystallized micritic calcite groundmass. It is not clear, if these phenomena can be related to shock deformation.

7.2 Possible evidence for impact melting of marls and limestones of the Neogene and Cretaceous bedrock formations

Possible evidence for impact melting, subsequent quenching and devitrification of the bedrock rocks is based on the fabrics and textures the polymict breccias: (1) groundmass-forming calcite within clasts exhibiting quenched feathery, arborescent and variolitic textures, (2) spheres with cryptocrystalline to microcrystalline, partially porcelain-like micro-fabrics, consisting either of pure calcite or fine mixtures of calcite-clay mineral assemblages, (3) carbonate and spheroidal particles, (4) mineral fragments of quartz and accessory minerals, such as zircon, (5) "immiscible" globules of calcite and iron oxides and sulfides in quartz, and in the (6) relict recrystallized "fluidal and curved glass fragments".

7.2.1 Calcite with feathery and arborescent textures

Feathery calcite crystallites (FC) are the major constituents in most of the Zerelia clasts, spheroidal particles and spheres. It seems that rapid crystallization of feathery calcite during quenching from a mainly calciocarbonate, and partly marly fluid environment does not permit the formation of ideal spheres. The spheroidal particles are

SED
5, 1511–1573, 2013

rather irregular shaped, oval, subrounded, and partly coagulated in clusters. The "ideal-shaped" carbonate spherules that are reported from several impact sites with melting of carbonates (e.g. Haughton crater, Osinski and Spray 2001) seem to have formed by immiscibility in pure silicate melts.

Feathery calcite aggregates, which occur as major constituents in spherules and have been reported in the proximal ejecta of sedimentary target rocks from several major impact sites: Ries (Graup, 1993; Osinski and Spray, 2004); Meteor crater Arizona (Osinski et al., 2003), Chicxulub (Jones et al., 2000; Clays et al., 2003; Schulte et al., 2009; Deutsch and Schulte, 2010); Alamo event (Pinto and Warme, 2008); Chesapeake Bay (Vanko, 2009). These crystallites are thought to represent quenched impact related products, thus indicative of rapid crystallization from a calciocarbonate melt.

7.2.2 Recrystallized "fluidal and curved glass fragments" in the carbonate clasts

Recrystallized "fluidal and curved glass fragments" as dense reddish and brownish submicroscopic patches of clay aggregate fragments have been recognized in several carbonate clasts from the walls of the larger Zerelia lake ZLW, which may exhibit calcium and magnesium-bearing silica melt compositions prior to devitrification (Table. 1). Figures 5g and h, 6d and e demonstrate the possible textural evidence of "glassy relicts". Such former glass shards might give ~~the~~ clue to understand the dynamic process and physical conditions of the shock-metamorphic, melting and quenching effects during impact into target limestones, shales and cherts of the bedrock.

In addition, devitrification and fluid circulation recognized in all breccias require near-surface alteration processes and precipitation of fine-grained mineral phases, which will be discussed in the final chapter.

SED
5, 1511–1573, 2013

7.2.3 Immiscible calcite globules in quartz

Globules are designated by their shape, size and composition. The most common analyzed globules in the polymict breccias from the Magoula Zerelia twin-lake craters are of calcite composition, irregular shapes from lenses to spheres and from nanometer to a few µm in size.

Carbonate-silicate liquid immiscibility has been reported in silicate-rich impact melt glasses from proximal ejecta of Chicxulub, Ries, Haughton, and Tenoumer craters (review in Osinski et al., 2008, 2011; Reimold et al., 2012). Similar immiscible calcite globules have been reported in the ejecta of a 200–100 ka meteorite impact from the Western Desert of Egypt by Osinski et al. (2005, 2007). Monomineralic calcite as irregular patches occurs within mixed-melt particles in the suevite glass of the German Steinheim crater (Anders et al., 2011). It has to be noted, that all the quenched calcite assemblages lack vesicular features, in contrast to silicate glasses, which could either be explained by a minor release of CO_2 gas or the escape of the gas phase during quenching to crystal aggregates.

Experimental data of Lee et al., (1994) indicate for a formation of round calcite globules in the system of CaO-SiO_2-CO_2 at pressures of 2.5 GPa and temperatures between 1200 and 1350 °C for equilibrium crystallization, forming dendritic (equal to feathery and arborescent textures) calcite crystal assemblages and intergrowth with quartz. Phase relations of $CaCO_3$ in the context of shock compression and decompression were re-evaluated by Ivanov and Deutsch (2002) with the conclusion that the liquid field had to be extended while the field of decomposition was narrowed down to low pressures. The main result of their work has been the extension of the liquid field of $CaCO_3$. This implies that an impact with pressures > 1 GPa and temperatures between > 1500 and 2000 K into carbonate sedimentary rocks is melting. Decomposition may only occur during cooling and decompression to atmospheric pressures and should release CO_2 and residual CaO (including MgO), which will transform mainly into calcite after cooling. No CaO has been recognized in all the x-ray diffraction pattern

SED
5, 1511–1573, 2013

of feathery calcite. Brooker and Kjarsgaard (2010) concluded according to advanced experimental data in the system SiO_2-Na_2O-Al_2O_3-CaO-CO_2 at 0.1–2.5 GPa and temperatures 1225–1700 °C, that such calcite globules may represent solid state calcite at high temperatures within an alkaline-rich environment and non-immiscible liquids, but real immiscible liquids in a low-alkali or alkali-free high SiO_2+Al_2O_3 system. The latter ~~seem to~~ be the case in the Zerelia breccias according to the SEM/EDX data.

7.2.4 Partial melting phenomena ~~of~~ ilmenite, rutile, spinel and zircon

The accessory mineral phases ilmenite, rutile, spinel and zircon occur as xenomorhic inclusions in fragmental quartz as well as between feathery and arborescent calcite matrices of spheres and spheroidal particles. They exhibit irregular, partly skeletal shapes with bulged rims and hollows ~~indicative for~~ high-temperature partial melting. In addition, several zircon fragments show indistinctly granular textures, which could be typical features ~~affected by high-pressure~~ impacts, according to Kamo et al. (1996), Corfu et al. (2003) and Toyer et al. (2012).

High-temperature melting-crystallization between 1240 and 1500 °C for Fe-Ti-oxid solid solutions has been shown experimentally in industrial furnaces using slags by Dierich et al. (2000) and with natural material by Zietsman and Pistorius (2004). High-temperature experiments of 700–900 °C and at 1 bar yielded crystallization of solid solutions between ilmenite ($FeTiO_3$) and pyrophanite ($MnTiO_3$) co-existing with metallic Fe and rutile (Feenstra and Peters, 1996). In nature, Mg- and Mn-bearing ilmenite has been found in mantle-derived kimberlites (e.g. Cruz et al., 2008; Kaminskya and Belousovab, 2009), the latter also in metamorphosed Mn-rich sedimentary and acid magmatic rocks.

SED
5, 1511–1573, 2013

7.3 The hypothetical meteorite impact (excavation, emplacement, deposition and alteration of impact ejecta)

A general hypothetical model for the Magoula Zerelia twin lakes as ~~typical~~ simple impact crater ~~has been given~~ (Fig. 12) using the approximate dimensions of the larger westerly lake and the obtained gravity data. Excavation, emplacement and deposition of the bedrock material must have followed the impact within seconds ~~as back-fall ejecta~~. Melting, quenching and vaporization may only have ~~been~~ taken place inside the plume and in the immediate vicinity of the impact. Several consecutive processes during the impact may have happened:

The heat and pressure wave of the projectile hit first the unconsolidated Holocene and poorly cemented porous Neogene sediments causing instant melting by decompression of the marly limestones. Fracturing and brecciation followed in the deeper levels of the compact Mesozoic crystalline limestones, shales, schists and cherts.

The variety of clasts and breccias must be therefore mainly the result chaotic turbulence. The intensive fracturing of quartz to micron-sized fragments without ~~strong~~ shock-metamorphic planar ~~structures~~ must have been due to decompression and melting of the carbonates. The different kinds of calcite crystallization: rapid quenching and subsequent crystallization to crypto-, micro-sparitic and euhedral calcite assemblages, is caused by the cooling rate and distance of the ejecta from the rather small impact environment. This ~~explains~~ the variations in the matrices of the breccias from rather dense feathery-rich carbonate breccias to more porous polymict breccias with cryptocrystalline to micro-sparitic carbonatic matrices.

All impact and emplacement processes: fracturing, brecciation, and excavation as well as melting and quenching must have been generated by a single instant event compared to many other known geological processes, which can produce similar products mainly within multiple events, such as volcanic pyroclastic deposits or hydroclastic ejecta. The ~~back-fall~~ impact ejecta may differ in distribution and size around an impact structure (Fig. 12): larger clasts, such as breccias comprise the crater fillings and prox-

SED
5, 1511–1573, 2013

imal walls, whereas smaller brecciated clasts and spheroidal particles must have been deposited in distal environments.

In general, the spheres and spheroidal particles could have been formed by different mechanical processes in an impact plume, as suggested e.g. by Langenhorst et al. (2000). In the case of the Magoula Zerelia crater, the carbonate spheres with concentric and spheroidal shapes may have been generated as a result of agglomeration of dust mineral and rock particles in or close to the turbulent expanding impact plume. Cementation of the spheroidal particles occurred during the turbulence by quenching of the carbonate melts as well as by hydration of carbonates due to post-impact surface and subsurface fluids. Ideally shaped spheroidal particles containing feathery, arborescent and even variolitic calcite crystallites have not been observed. It seems that feathery calcite forming during quenching does not permit the formation of an ideal spheres, they are rather irregular shaped, oval, subrounded, and partly coagulated in clusters. Independently, the quartz spheroidal particles may have been formed from partial melted cherts and quartz lenses by condensation of highly viscous quartz liquids, a process proposed by Salge et al. (2002) for the accretionary lapilli formed by the large Chicxulub impact.

The amount of vaporization and release of gas, e.g. CO_2 is unknown, since there is no data up to now on the existing fluid inclusions in calcite and quartz.

In addition, a rather wet environment must have been generated by the decomposition of clayey and marly sediments due to high temperatures after pressure release. Therefore, fluid circulation must have occurred during and subsequent to the impact within the crater fillings. Any carbonatic hydraulic flow is usually due to hydrothermal circulation. This is evident by the presence of different generations of calcite veins in the clasts and spheres as well in the appearance of fluid inclusions in quartz. This refers to both, quartz fragments with irregular shapes, rounded, subrounded, and xenomorphic quartz with bulged rims as well as in quartz with idiomorphic shapes. The formation of disseminated veins of micro-sparitic calcite, smectite, and crypto-crystalline, partly dendritic iron (goethite) and manganese oxides as well as iron and manganese coating

SED
5, 1511–1573, 2013

of many concretions as part of all Zerelia clasts must have taken place under surface and subsurface conditions. In addition, injection under pressure, breaking rock fragments and quartz, contributes to brecciation.

8 Conclusions

Detailed petrographic and mineralogical studies (optical microscopy, scanning electron microscopy, Raman spectroscopy, X-ray diffraction) on a large number of samples from millimeter to decimeter rock size confirmed the results of the preliminary investigation (Dietrich and Gartzos, 2009): the unusual polymict breccias with abundant chert fragments, deformed and highly fragmented quartz, calcite with feathery and microsparitic textures, spheres and spheroidal particles, calcite globules in quartz, ~~lead to the evidence of a rather~~ weak shock-metamorphism ~~but~~ melting. Decompression of the unconsolidated Holocene and poorly cemented, porous water bearing Neogene sediments must have caused an increase of temperature and thus, instant melting. The most convincing evidence is the finding of partial melted zircon with granular ~~deformation~~, f[illegible]mental ilmenite and rutile for which temperatures of 1240 up to 1800 °C are required, which do not occur in metamorphic and magmatic processes within the earth crust and the uppermost mantle. Minuscule globules of calcite are present in quartz fragments, and thus might represent recrystallized immiscible melts between SiO_2 and $CaCO_3$. In addition, improperly identifiable Al-Si- and sulfur bearing Fe-phases as globules < 1 to ~~10~~ µm in size, have been found in quartz, spheres and globules, similar to Fe-phases reported in the ejecta from several impact craters worldwide and in some meteorites.

All the clasts and breccias could be ~~considered~~ as "impact ~~back-fall~~ breccia and carbonate lapilli" ~~due to an impact~~, although up to now no meteorite fragments have been found. Further mineralogical identification and precise trace element analyses of the feathery and cryptocrystalline matrix calcite, of the quartz fragments, of the miniscule

SED
5, 1511–1573, 2013

Fe-particles, spheroidal particles and globules may elucidate the origin of the projectile, iron or stone meteorite.

The only remaining chemical tracer criteria, derived from fourteen selected samples by X-ray fluorescence analyses of the Zerelia ejecta, of an impact fro partially dis-
integrated iron meteorite could be the o rence of nickel besides iron. However, the enriched Ni content compared to similar amounts of Cr and the low values of magnesium point to a possible source of an iron meteorite ~~than to~~ a contamination from the very rare basic and ultrabasic fragments in the breccias. However, iron-nickel and magnetite globules and spheroidal particles ~~with sizes of a few µm up to approximately 100 µm~~ in unconsolidated ejecta and in the clasts and breccias have not yet been found. The weak magnetic anomalies in the relict walls of the craters indicate their possible existence but show no evidence of a major magnetic body beneath the lakes.

The modeled "Residual Gravity Profiles" through the larger western lake indicate a negative gravity anomaly, showing a bowl-type structure in a form of a crater as depicted by the density contrast tomography. An equivalent crater structure was modeled with strong negative residual gravity anomaly over the eastern lake. However, in detail the residual gravity anomalies models between the two lakes differ significantly from each other. The anomaly of the western lake seems to be smaller, the penetration less deep between 100 and 200 m. In contrast, the gravity anomaly of the eastern lake appears to be larger, reaching a depth between 200 to 300 m. The form and shape of the above negative gravity anomalies are consistent with those in other areas of the world, where meteorite impacts occurred, as the Steinheim impact meteorite crater in southern Germany. The negative gravity/density anomalies underneath the lakes are the result of a combination of unconsolidated mud, a mixture of clay-rich detrital sediments in the upper part and a highly shattered brecciated zone of allochtonous debris fillings in the lower part. This situation also explains the impermeability of the craters and thus, the lack of drainage.

The magnetic anomalies might reflect a combination relict magnetite fragments, found in spheres, clasts and breccias, with the possibility of existence of millimeter-

SED
5, 1511–1573, 2013

sized globules and spheroidal particles consisting of iron-nickel and magnetite-maghemite composition, similar to their occurrence in the Neolithic Morasko crater field in northern Poland (Stankowski et al., 2002, 2006). The unusual, rather constant trace element content of nickel in all analyses of the Zerelia ejecta indicates such a possibility. However, in conclusion, the magnetic measurements did not seem to support the presence of definite relics of iron meteorites at depth.

The morphology and dimensions of the Zerelia lakes limit the physical conditions of a hypervelosity meteorite impact (French, 1998; Kenkmann et al., 2005, 2009; Turtle et al., 2005; Osinski et al., 2008; and in the "Earth Impact Database"). According to the knowledge from all known and well established meteorite impact structures, the dimensions of the meteorite, which might have split into two fragments, could have been about 10–30 m before reaching the surface.

The temperature > 1000 °C and pressure not exceeding 10 GPa of the impact may have been sufficient to brecciate and partially melt the limestones by decompression at temperatures followed by quenching during cooling to form the unusual carbonate clasts.

Appendix A

Analytical procedures

During four sampling campaigns 2008 and 2010 a large variety of 240 samples has been collected for petrographic and geochemical studies: clasts and breccias from few centimeters to approximately 20 cm in size, several kilograms grab samples of gravel and sand as well as 4 drill samples from the only two small outcrops Sp1 and Sp2 south and north of the larger Zerelia Lake West (Figs. 1, 4a and b). The petrographic description is based on 50 thin sections and 20 polished sections containing numerous grains, several mm in size.

SED
5, 1511–1573, 2013

The mineral species were identified by optical microscopy in thin section of 10 to 20 µm thickness, X-ray diffraction (XRD) on smear slides and bulk powder samples, and Raman spectroscopy. In addition, chemical qualitative as well as quantitative elemental abundances were determined for some SEM samples by energy-dispersive X-ray spectrometry (EDS).

The Institute of Geochemistry and Petrology operates the following analytical instruments, most of them the latest generation.

JSM-6390LA analytical scanning microscope

Scanning Electron Microscopy (SEM) imaging was applied to study textures and chemical compositions of cryptocrystalline, microcrystalline groundmass as well as the pseudomorph glassy fragments and partial melted minerals. A JEOL JSM-6390LA, high-performance scanning electron microscope was used for fast characterization and imaging of fine structures, which enabled analysis in rock thin sections of 27 mm × 47 mm size. The images were taken with a high resolution at 1.2-1.6 nÅ at 15 kV, ~~the JSM-6390LA delivers amazing clarity of the finest structures~~. In addition to routine imaging at several hundreds of times greater resolution than the optical microscope, and with a focal depth several tens of times greater than the optical microscope, the SEM allowed for detailed measurements. An optional energy dispersive X-ray spectrometer (EDS) provided elemental analysis.

Raman spectroscopy

Two different micro-Raman spectrometers were used: a DILOR Labram instrument equipped with an Olympus microscope an internal He-Ne laser and an external Ar-ion laser. Three exciting wavelengths were available: 488 nm, 514.5 nm, 632 nm. Currently we run the instrument at 514.5 nm. Diameter of laser beam < 1 µm and a Horiba Jobin Yvon at a 532.12 excitation with a CCD1 detector and 100x magnification, at 20 s time.

SED
5, 1511–1573, 2013

The analyses were performed on polished rock thin sections of approx. 20–30 mm thickness.

X-ray Powder Diffraction (XRD)

Powder X-ray diffractometer (Bruker, AXS D8 Advance), equipped with a Lynxeye superspeed detector and an automatic sample changer for 9 samples for the identification of mineral species.

X-ray Fluorescence Analysis (XRF)

Wave-length dispersive X-ray fluorescence spectrometer (WD-XRF, Axios, PANalytical, 2.4 kW sequential, rhodium radiation, 20–60 kV, 40–100 mA, automatic sample changer), equipped with 5 diffraction crystals for bulk chemical analysis of rocks. Standard analyses are performed on fused glass-beads prepared from rock powder mixed with lithium-tetraborate (1 : 5 mixture) using a Claisse M4® fluxer. A minimum of 1 g of fired rock powder is required. The current setup includes 10 major (SiO_2, TiO_2, Al_2O_3, Fe_2O_3, MnO, MgO, CaO, Na_2O, K_2O, P_2O_5) and 21 trace elements (S, Sc, V, Cr, Co, Ni, Cu, Zn, Ga, Rb, Sr, Y, Zr, Nb, Ba, La, Ce, Nd, Pb, Th, U). The calibration ~~bases~~ on 33 certified international standards with emphasize on igneous and metamorphic rock compositions (PW 2450- super Q, Zurich application Traces, 2011). However, for the ~~case of~~ bulk analysis of the Zerelia carbonatitic breccias, a calibration for sedimentary (mainly carbonate) rocks was used.

Acknowledgements. We thank the 13th Ephoret of Prehistoric and Classical Antiquities (Volos, Greece) for permission of sampling in the neighborhood of the prehistoric site Magoula Zerelia; E. Chatzikyriakos, the major of the community of Almiros, who permitted the excavation of a trench and provided the necessary machinery; Lydia Zehnder for running XRD and XRF samples and Thomas Good for preparation of thin sections and SEM mounts (Institute of Geochemistry and Petrology, ETH Zurich, Switzerland); S. Chailas (National and Kapodistrian University of Athens, Greece) for his contribution in gravity modeling; John S. Latsis Public

Benefit Foundation Project 2010 (Athens, Greece) for financial support, and Alexander Deutsch (Universität Münster, Germany) for fruitful discussions.

References

Anders, D., Kegler, P., Buchner, E., and Schmieder, M.: Carbonate melt lithologies from the Steinheim impact crater (SW Germany), 42nd Lunar and Planetary Science Conference, 1997, 2011.

Alvarez, L. W., Alvarez W., Asaro, F., and Michel, H. V.: Extraterrestrial cause for the Cretaceous-Tertiary extinction, Science, 208, 1095–1108, 1980.

Alvarez, W., Claeys, P., and Kieffer, S. W.: Emplacement of Cretaceous-Tertiary boundary shocked quartz from Chicxulub crater, Science, 269, 930–935, 1995.

Bischoff, A., Scott, E. R. D., Metzler, K., and Goodrich, C. A.: Nature and origins of meteoritic breccias, in: Meteorites and the Early Solar System II, edited by: Lauretta, D. S. and McSween Jr., H. Y., Univ. Arizona Press, 679–712, 2006.

Brooker, R. A.: The effect of CO_2 saturation on immiscibility between silicate and carbonate liquids, an experimental study, J. Petrol., 39, 1905–1915, 1998.

Brooker, R. A. and Kjarsgaard, B. A.: Silicate-carbonate liquid immiscibility and phase relations in the system SiO_2-Na_2O-AZLWO_3-CaO-CO_2 at 0.1–2.5 GPa with application to carbonatite genesis, J. Petrol., 1–25, 2010.

Burt, J. B., Pope, K. O., and Watkinson, A. J.: Petrographic, X-ray diffraction and electron spin resonance analysis of deformed calcite: meteor crater, Arizona, Meteorit. Planet. Sci., 40, 296–305, 2005.

Caputo, R.: Geological and structural study of the recent and active brittle deformation of the Neogene-Quaternary basins of Thessaly (Central Greece), Ph.D. thesis, University of Flornce, Sci. Ann. Aristotle University Thessaloniki, 12, vol. 2, 1–252, 1990.

Caputo, R.: The active Nea Anchialos Fault System (Central Greece): comparison of geological, morphotectonic, archaeological and seismological data, Annali di Geofisica, 39, 557–574, 1996.

Clark, J. F.: Magnetic survey data at meteoritic impact sites in North America, Geomagnetic Service of Canada, Earth Physics Branch, Open File, 83, 5, 1–32, 1983.

Corfu, F., Hanchar, J. M., Hoskin, P. W. O., and Kinny, P.: Atlas of zircon textures, Rev. Mineral. Geochem., 53, 469–500, 2003.
Cruz, S. R., Watangua, M., Melgareio, J. C., and Gali, S.: New insights into the concept of ilmenite as an indicator for diamond exploration, based on kimberlite petrographic analysis, Macla 9, September 2008, Revista de la Sociedad Espaniola de Mineralogia, 205–206, 2008.
Deutsch, A. and Schulte, P.: Carbonates in the proximal ejecta deposits of the K/T Chicxulub impact crater, 41st Lunar and Planetary Science Conference 2010.
Dierich, J.-C., Bauer, W., and Fünders, D.: Synthetic Titanium slags in Furnaces, 12 pp., available at: www.sachtleben.de/publications/0090e072.pdf, 2000.
Dietrich, V. J. and Gartzos, E.: Twin meteorite impact craters in Thessaly Central Greece of Holocene age, Proceedings of the 7th Swiss Geoscience Meeting, Neuchâtel, November 2009.
Dunham, R. J.: Classification of carbonate rocks according to depositional texture, in: Classification of carbonate rocks, edited by: Ham, W. E., American Association of Petroleum Geologists, Memoir, 1, 108–121, 1962.
Earth Impact Database last update 12 December: Planetary and Space Science Centre, University of Brunswick, Canada, available at: http.//www.passc.net/EarthImpactDatabase/index.html, 2013.
Ernstson, C.: A gravity-derived model for the Steinheim impact structure, Geol. Rundsch., 73, 483–498, 1984.
Evans, K. R., Horton Jr., J. W., King Jr., D. T., and Morrow, J. R. (Eds.): The sedimentary Record of Meteorite Impacts, Geological Society America, Special Paper, 437, 2008.
Feenstra, A. and Peters, T.: Experimental determination of activities in $FeTiO_3$-$MnTiO_3$ ilmenite solid solution by redox reversals, Contrib. Mineral. Petrol., 126, 109–120, 2002.
French, B. M.: Traces of Catastrophe, a Handbook of Shock-Metamorphic Effects in Terrestrial Meteorite Impact Structures, LPI Contribution 954, Lunar and Planetary Institute, Houston, 120 pp., 1998.
French, B. M. and Koeberl, C.: The convincing identification of terrestrial meteorite impact structures. What works, what does not, and why, Earth-Sci. Rev., 98, 123–170, 2010.
Gasperini, L., Bonatti, E., and Longo, G.: Reply – Lake Cheko and the Tunguska Event: impact or non-impact?, Terra Nova, 20, 169–172, 2008.

SED
5, 1511–1573, 2013

Gasperini, L., Cocchi, L., Stanghellini, C., Stanghellini, G., Del Bianco, F., Serrazanetti, M., and Carmisciano, C.: Magnetic and seismic reflection study of Lake Cheko, a possible impact crater for the 1908 Tunguska Event, Geochem. Geophy. Geosy., 13, Q05008, doi:10.1029/2012GC004054, 2012.

Gibson, R. L. and Reimold, W. U. (Eds.): Large Meteorite Impacts and Planetary Evolution IV., Geological Society America Special Paper 465, 660 pp., 2010.

Graup, G.: Carbonate-silicate liquid immiscibility upon impact melting, Ries Crater Germany, Meteorit. Planet. Sci., 34, 425–438, 1999.

Gurov, E. P. and Gurova, E. P.: The group of Macha crater in western Yakutia, Planet. Space Sci., 46, 323–328, 1998.

Hamers, M. F. and Drury, M. R.: Scanning electron microscope-cathodoluminescence (SEM-CL) imaging of planar deformation features and tectonic deformation lamellae in quartz, Meteorit. Planet. Sci., 46, 1814–183, 2011.

Henkel, H. and Pesonen, L. J.: Impact craters and craterform structures in Fennoscandia, Tectonophysics, 216, 31–40, 1992.

Hipkin, R. G. and Lagios, E.: A Fortran-IV program for the estimation of the Bouguer Density by fitting trend surfaces to the Bouguer anomaly, Public. No. 80–3, Geophysics Dept. Edinburgh University, Edinburgh, UK, 14 pp., 1980.

Hipkin, R. G., Lagios, E., Lyness, D., and Jones, P.: Reference gravity stations on the IGSN'71 standard in Britain and Greece, Geophys. J. Int., 92, 143–148, 1988.

Hoernle, K., Tilton, G., LeBas, M. J., Duggen, S., and Garbe-Schönberg, D.: Geochemistry of oceanic carbonatites compared with continental carbonatites: mantle recycling of oceanic crustal carbonate, Contrib. Mineral. Petrol., 142, 520–542, 2002.

Hosein, F.: Mud volcanoes in the mobile shale basin of the Trinidad area with special focus on the spectacular eruption of the Piparo mud volcano, AAPG/GSTT Hedberg Conference, "Mobile Shale Basins – Genesis, Evolution and Hydrocarbon Systems", 4–7 June 2006, Port of Spain, Trinidad and Tobago, available at: http://www.searchanddiscovery.com/abstracts/html/2006/hedberg_intl/abstracts/hosein.htm, 2006.

Innocenti, F., Manetti, P., Peccerillo, A., and Poli, G.: Inner arc volcanism in NW Aegean arc: geochemical and geochronological data, Neues Jb. Miner. Monat., 145–158, 1979.

Ivanov, B. A. and Deutsch, A.: The phase diagram of $CaCO_3$ in relation to shock compression and decompression, Phys. Earth Planet. Inter., 129, 131–143, 2002.

Jones, A. P., Langenhorst, F., Claeys, P., and Heuschkel, S.: Impact melting of carbonates from Chicxulub Crater, in: Impacts and the Early Earth, Lecture Notes in Earth Sciences, 91, edited by: Gilmour, L. and Koeberl, C., Springer Verlag, 343–361, 2000.
Kaminskya, F. V. and Belousovab, E. A.: Manganoan ilmenite as kimberlite/diamond indicator mineral, Russian Geol. Geophys., 50, 1212–1220, 2009.
Kamo, S. L., Reimold, W. U., Krogh, T. E., and Colliston, W. P.: A 2023 Ma age for the Vredefort impact event and observations from shocked metamorphosed zircons in pseudotachylite breccias and granophyre, Earth Planet. Sci. Lett., 144, 369–388, 1996.
Keller, J.: Carbonatitic volcanism in the Kaiserstuhl alkaline complex: evidence for highly fluid carbonatitic melts at the earth's surface, J. Volcanol. Geoth. Res., 9, 423–431, 1981.
Keller, M.: Die Sedimente der Zwillings-Impaktkraterseen in Thessalien, Griechenland, Semesterarbeit FS 2010, Dept. Environmental Sciences, ETH Zurich, Switzerland, 53 pp., in German, 2010.
Kenkmann, T., Artemieva, N. A., Wünnemann, K., Poelchau, M. H., Elbeshausen, D., Núñez, and Del Prado, H.: The Carancas meteorite impact crater, Peru, geologic surveying and modeling of crater formation and atmospheric passage, Meteorit. Planet. Sci., 44, 985–1000, 2009.
Kenkmann, T., Hörz, F., and Deutsch, A.: Large Meteorite Impacts III, Geological Society America, Special Paper 384, 2005.
Lagios, E., Chailas, S., and Hipkin, R. G.: Gravity and Isostatic Anomaly Maps of Greece produced, EOS Transaction, American Geophysical Union, 76, 274 pp., 1995.
Lagios, E., Chailas, S., and Hipkin, R. G.: Newly compiled gravity and topographic data banks of Greece, Geophys. J. Int., 126, 287–290, 1996.
Langenhorst, F., Deutsch, A., Ivanov, B. A., and Hornemann, U.: On the shock behavior of $CaCO_3$, Dynamic loading and fast unloading experiments – modeling mineralogical observations, Lunar and Planetary Science Conference, 31, 1851 pp., 2000.
Lee, W.-J., Wyllie, P. J., and Rossman, G. R.: CO_2-rich glass, round calcite crystals, and no liquid immiscibility in the system CaO-SiO_2-CO_2, at 2.5 GPa, Am. Mineral., 79, 1135–1144, 1994.
Liu, F., Colombo, C., Adamo, P., He, J. Z., and Violante, A.: Trace elements in manganese-iron nodules from a Chinese alfisol, division S-9, soil mineralogy, Soil Sci. Soc. Am. J., 66, 661–670, 1962.

SED
5, 1511–1573, 2013

Marinos, G., Anastopoulos, J., Maratos, G., Melidonis, N., and Andronopoulos, B.: Geological Map of Greece, 1 : 50 000, sheet Anavra, Institute for Geology and Subsurface Research, Athens, 1957.
Marinos, G., Anastopoulos, J., Maratos, G., Melidonis, N., and Andronopoulos, B.: Geological Map of Greece, 1 : 50 000, sheet Almiros, Institute for Geology and Subsurface Research, Athens, 1962.
Marinou, G.: Sur deux volcans embryonnaires du type mare, prés d'Almiros-Thessalie, Bull. Geol. Soc. Greece, 5, 108–114, 1963.
Marinos, G. and Papakis, N.: Sur deux petits lacs "Zileria" près d'Almiros-Thessalie, Geol. Geosphys. Res., 9, 175–194, 1965.
Mourão, C., Mata, J., Doucelance, R., Madeira, J., da Silveira, A. B., Silva, L. C., and Moreira, M.: Quaternary extrusive calciocarbonatite volcanism on Brava Island (Cape Verde), a nephelinite-carbonatite immiscibility product, J. African Earth Sci., 56, 59–74, 2010.
Ormö, J., Rossi, A. P., and Komatsu, G.: The Sirente crater field, Italy, Meteorit. Planet. Sci., 37, 1507–1523, 2002.
Ormö, J., Gomez-Ortiz, D., McGuire, P. C., Henkel, H., Komatsu, G., Angelo, P., and Rossi, A.: Magnetometer survey of the proposed Sirente meteorite crater field, central Italy: evidence for uplifted crater rims and buried meteorites, Meteorit. Planet. Sci., 42, 211–222, 2007.
Ormö J., Koeberl, C., Rossi, A. P., and Komatsu, G.: Geological and geochemical data from the proposed Sirente crater field: new age dating and evidence for heating of target, Meteorit. Planet. Sci., 41, 1331–1345, 2007.
Osinski, G. R.: Impact metamorphism of $CaCO_3$-bearing sandstones at the Haughton structure, Canada, Meteorit. Planet. Sci., 42, 1945–1960, 2007.
Osinski, G. R. and Spray, J. G.: Impact-generated carbonate melts, evidence from the Haughton structure, Canada, Earth Planet. Sc. Lett., 194, 17–29, 2001.
Osinski, G. R., Buch, T. E., and Wittke, J.: Evidence for shock melting of carbonates from Meteor Crater, Arizona, 66th Meteoritical Society meeting, Münster Germany, abstract 5070, 2003.
Osinski, G. R., Grieve, R. A. F., and Spray, J. G.: The nature of the groundmass of surficial suevite from the Ries impact structure, Germany, and constraints on its origin, Meteorit. Planet. Sci., 39, 1655–1683, 2004.
Osinski, G. R., Schwarcz, H. P., Smith, J. R., Kleindienst, M. R., Haldemann, A. F. C., and Churcher, C. S.: Evidence for a 200–100 ka meteorite impact in the Western Desert of Egypt, Earth Planet. Sc. Lett., 253, 378–388, 2007.

SED
5, 1511–1573, 2013

Osinski, G. R., Spray, J. G., and Grieve, R. A. F.: Impact melting in sedimentary target rocks, an assessment, in: The Sedimentary Record of Meteorite Impacts, edited by: Evans, K. R., Horton Jr., J. W., King Jr., D. T., and Morrow, J. R., Geological Society of America Special Paper, 437, 1–8, 2008.

Osinski, G. R., Spray, J. G., and Lee, P.: Impactites of the Haughton impact structure, Devon Island, Canadian High Arctic, Meteorit. Planet. Sci., 40, 1789–1812, 2005.

Osinski, G. R., Tornabene, L. L., and Grieve, R. A. F.: Impact ejecta emplacement on terrestrial planets. Earth Planet. Sc. Lett., 310, 167–181, 2011.

Papazachos, B. C., Panagiotopoulos, T. M., Tsapanos, D. M., Mountrakis, D. M., and Dimopoulos, G. C.: A study of the summer seismic sequence in the Magnesia region Central Greece, J. Roy. Astronom. Soc., 75, 155–168, 1983.

Pe-Piper, G. and Piper, D. J. W.: The geological significance of manganese distribution in Jurassic-Cretaceous rocks rocks of the Pindos basin, Peloponnnese, Greece, Sediment. Geol., 65, 127–137, 1989.

Pilkington, M. and Grieve, R. A. F.: The geophysical signature of terrestrial impact craters, Rev. Geophys., 30, 161–181, 1992.

Pinto, J. A. and Warme, J. E.: Alamo Event, Nevada, crater stratigraphy and impact breccia Realms, Geol. S. Am. S., 437, 99–137, 2008.

Raukas, A., Punning, J.-M., Moora, T., Kestlane, U., and Kraut, A.: The structure and age of the Kaali main crater, Island of Saaremaa, Estonia, Impact Stud., 341–355, 2005.

Raukas, A., Tiirmaa, R., Kaup, E., and Kimmel, K.: The age of the Ilumetsa meteorite craters in southeast Estonia, Meteorit. Planet. Sci., 36, 1507–1514, 2001.

Reimold, W. U., Hansen, B. K., Jacob, J., Artemieva, N. A., Wünnemann, K., and Meyer, C.: Petrography of the impact breccias of the Enkingen (SUBO 18) drill core, southern Ries crater, Germany: new estimate of impact melt volume, Geol. Soc. Am. Bull., 124, 104–132, 2012.

Reinders, H. R. (Ed.): Prehistoric Sites at the Almiros and Sourpi Plains Thessaly, Greece, Royal Van Gorcum and Comp., Assen, the Netherlands, 166 pp., 2004.

Reinders, R. and Bottema, S.: Investigations at Halos and Zerelia, preliminary report, Babesch Bull. Ant. Bes., 58, 91–100, 1983.

Robertson, A. H. F. and Varnavas, S. P.: The origin of hydrothermal metalliferous sediments associated with the Early Mesozoic Othris and Pindos ophiolites, mainland Greece, Sediment. Geol., 53, 87–113, 1993.

Salge, T., Tagle, R., and Claeys, R.: Accretionary Lapilli from the KT Boundary site of Guayal, Mexico: preliminary insights of expansion plume formation, 63rd Annual Metoritical Society Meeting, available at: www.lpi.usra.edu/meetings/metsoc2000/pdf/5124.pdf, 2000.
Schulte, P., Deutsch, A., Salge, T., MacLeod, K. G., Neuser, R. D., Kontny, A., and Krumm, S.: A dual-layer Chicxulub ejecta sequence with shocked carbonates from the Cretaceous-Paleogene (K-Pg) boundary, ODP Leg 207, Demerara Rise, western Atlantic, Geochim. Cosmochim. Ac., 73, 1180–1204, 2009.
Sheldon, N. D.: Do red beds in dicate paleoclimatic conditions? A Permian case study, Paleogeogr. Paleoclim. Paleoecol., 228, 305–319, 2005.
Shoemaker, E. M. and Chao, E. C. T.: New evidence for the impact origin of the Ries Basin, Bavaria, Germany, J. Geophys. Res., 66, 3371–3378, 1961.
Smith, A. G., Hynes, A. J., Menzies, M., Nisbet, E. G., Price, I. Welland, M. J. P., and Ferrière, J.: The stratigraphy of the Othris Mountains, eastern central Greece: a deformed Mesozoic continental margin sequence, Ecol. Geol. Helvet., 68, 463–481, 1975.
Speranza, F., Sagnotti, L., and Rochette, P.: An anthropogenic origin of the "Sirente crater," Abruzzi, Italy, Meteorit. Planet. Sci., 39, 635–649, 2004.
Stähle, V., Altherr, R., Koch, M., and Nasdala, L.: Shock-induced growth and metastability of stishovite and coesite in lithic clasts from suevite of the Ries impact crater (Germany), Contrib. Mineral. Petrol., 155, 457–472, 2008.
Stankowski, W., Muszyñskia, A., Klimmb, K., and Schliestedt, M.: Mineralogy of Morasko meteorite and the structure of the craters, Proc. Estonian Acad. Sci. Geol., 51, 227–240, 2002.
Stankowski, W. T. J., Katrusiak, A., and Budzianowski, A.: Crystallographic variety of magnetic spherules from Pleistocene and Holocene sediments in the northern foreland of Morasko-Meteorite reserve, Planet. Space Sci., 54, 60–70, 2006.
Stoppa, F.: The Sirente crater, Italy, impact vs. mud volcano origins, Meteorit. Planet. Sci., 41, 467–477, 2006.
Stoppa, F. and Lupini, L.: Mineralogy and petrology of the Polino Monticellite Calciocarbonatite Central Italy, Mineral. Petrol., 49, 213–231, 1993.
Theocharis, R. D.: Neolitic Greece, National Bank of Greece, 1973.
Therriault, A. M., Grieve, R. A. F., and Pilkington, M.: The recognition of terrestrial impact structures, Bull. Czech Geol. Surv., 77, 253–263, 2002.
Tohver, E., Lana, C., Cawood, P. A., Fletcher, I. R., Jourdan, F., Sherlock, S., Rasmussen, B., Trindade, R. I. F., Yokoyama, E., Souza Filho, C. R., and Marangoni, Y.: Geochronological

SED
5, 1511–1573, 2013

constraints on the age of a Permo–Triassic impact event: U-Pb and $^{40}Ar/^{39}Ar$ results for the 40 km Araguainha structure of central Brazil, Geochim. Cosmochim. Ac., 86, 214–227, 2012.

Trepmann, C. A.: Shock effects in quartz, compression vs. shear deformation – an example from the Rochechouart impact structure, France, Earth Planet. Sc. Lett., 267, 322–332, 2008.

Vanko, D. A.: A petrographic and fluid inclusion assessment of hydrothermal alteration of some impactites and crystalline rocks in the Chesapeake Bay impact structure, ICDP-USGS Eyreville-B core, in: The ICDP-USGS Deep Drilling Project in the Chesapeake Bay Impact Structure: Results from the Eyreville Coreholes, edited by: Gohn, G. S., Koeberl, C., Miller, K. G., and Reimold, W. U., Geol. S. Am. S., 458, 543–557, 2009.

Veski, S., Heinsalu, A., Kirsimäe, K., Poska, A., and Saarse, L.: Ecological catastrophe in connection with the impact of the Kaali meteorite about 800–400 BC on the island of Saaremaa, Estonia, Meteorit. Planet. Sci., 36, 1367–1376, 2001.

Veski, S., Heinsalu, A., Lang, V., Kestlane, E., and Possnert, G.: The age of the Kaali meteorite craters and the effect of the impact on the environment and man: evidence from inside the Kaali craters, island of Saaremaa, Estonia, Veget. Hist. Archaeobot., 13, 197–206, 2004.

Yancey, T. E. and Guillemette, R. N.: Carbonate accretionary lapilli in distal deposits of the Chicxulub impact event, Geol. Soc. Am. Bull., 120, 1105–1118, 2008.

Zietsman, J. H. and Pistorius, P. C.: Process mechanisms in ilmenite smelting, The Journal of the South African Institute of Mining and Metallurgy, December 2004, online, 653–660, 2004. (published: Journal of the SAIMM, 105, 4, pp. 229, 2005)

Table 1. Bulk rock chemical compositions from the breccias of the Zerelia twin lakes. LOI = loss of ignition; LLD = lower limit of detection; n.d. not determined. * Note: samples AS1, Alm16, Alm17, Alm18, ZLW2, M, and E major element analyses obtained only on 10 g powder pills of 4 cm diameter. The major element compositions are to high, since the powder pills were not ignited, and CO_2 not determined.

Samp. wt.%		AS 1 clast	D 11 clast	F 22 clast	Alm16 clast feather calcite	Alm17 clast crypto calcite	Alm18 clast crypto calcite	ZLW2 drill samp.	ZLEM limest.	ZLEE limest.
SiO_2		20.50	29.93	34.26	15.52	13.93	14.69	28.29	5.88	5.32
TiO_2		0.39	0.45	0.35	0.34	0.30	0.32	0.61	0.07	0.06
Al_2O_3		5.50	4.59	5.71	4.98	4.02	4.72	8.45	0.92	0.90
Fe_2O_{3tot}		3.49	2.08	2.10	3.09	2.82	8.27	5.25	1.36	1.40
MnO		0.12	0.45	0.11	0.37	0.48	0.43	0.26	0.09	0.03
MgO		0.85	0.65	0.90	0.81	1.20	0.96	1.27	0.42	0.48
CaO*		56.47	31.99	28.28	58.86	59.39	56.69	43.32	71.95	72.19
Na_2O		0.12	0.16	0.19	0.13	0.12	0.110	0.14	0.10	0.10
K_2O		0.66	0.57	0.74	0.59	0.61	0.48	0.97	0.13	0.12
P_2O_5		0.05	0.08	0.36	0.04	0.05	0.07	0.06	0.03	0.05
LOI		n.d.	28.14	25.43	n.d.	n.d.	n.d.	n.d.	n.d.	n.d.
total ppm/LLD		88.00	99.09	98.43	86.58	82.92	86.74	88.62	80.95	80.65
Ba	7	160	678	228	454	510	707	258	< 14	14
Sr	1	54	60	103	59	61	137	123	94	91
Rb	1	41	51	62	43	41	45	67	10	10
Nb	2	5	10	15	6	7	8	8	< 2	< 2
Zr	2	82	147	145	68	72	66	107	26	21
Y	1	31	36	96	81	46	71	25	11	26
La	11	70	59	102	136	113	133	45	< 11	< 11
Ce	5	30	48	108	107	93	97	39	< 5	< 5
Nd	5	20	22	50	57	45	54	20	< 5	< 5
Cr	3	86	174	252	88	105	101	154	50	36
Ni	3	89	86	108	85	220	94	134	66	53
V	3	98	91	99	88	156	93	118	56	59
Co	2	18	20	19	24	53	28	25	9	7
Cu	2	50	52	36	51	47	28	56	41	42
Zn	2	34	43	63	38	45	44	56	11	11
Pb	2	31	31	34	34	67	52	31	30	28
Sc	4	28	21	21	34	31	31	27	< 4	< 4
F	40	369	344	510	354	< 40	< 40	467	263	253
Cl	3	31	65	n.d.	49	20	49	23	81	24
S	10	< 10	< 10	125	< 10	< 10	218	16	< 10	< 10

SED
5, 1511–1573, 2013

Table 2. Bulk rock chemical compositions from 1 kg unconsolidated subsurface grab samples of unconsolidated subsurface breccias of the Zerelia twin lakes. LOI = loss of ignition; LLD = lower limit of detection; n.d. not determined. * Note: the major element analyses of all samples were only obtained on 10 g powder pills of 4 cm diameter. The major element compositions of ZLE1, ZLE2, ZLW1, ZLW2, and ZLWD are to high, since the powder pills were not ignited, and CO_2 not determined. ZLWS-1 silt, decarbonated silt, and clay represent grain size fractions of the grab sample ZLW1.

Samp. wt.%		ZLE1 sand total	ZLE2 sand fract. decarb.	ZLWD1 drill sample	ZLW1 sand fract.	ZLW2 sand fract.	ZLWS1 grab silt total	ZLWS1. silt fract. decarb.	ZLWS1 clay fract. total
TiO_2		0.70	0.43	0.54	0.87	0.82	0.33	0.79	0.80
Al_2O_3		9.51	8.16	12.28	15.91	15.00	5.54	12.15	13.92
Fe_2O_{3tot}		5.45	3.89	5.64	6.86	6.84	4.58	7.05	6.63
MnO		0.16	0.17	0.20	0.17	0.15	0.06	0.05	0.10
MgO		1.92	0.98	1.47	1.76	1.51	2.33	2.70	3.38
CaO*		33.10	5.56	2.25	13.54	16.22	30.69	1.08	9.30
Na_2O		0.32	< 0.10	0.22	0.14	0.16	1.00	2.12	1.45
K_2O		1.28	1.16	1.64	1.94	1.72	0.91	1.79	2.64
P_2O_5		0.19	0.10	0.07	0.15	0.13	0.04	0.04	0.12
LOI		n.d.	n.d.	n.d.	n.d.	n.d.	28.11	6.00	13.19
total ppm	LLD	87.78	92.76	89.93	94.77	94.09	98.20	100.78	99.75
Ba	7	368	258	250	344	337	131	225	332
Sr	1	268	32	34	59	55	1472	83	299
Rb	1	79	53	72	98	92	40	73	110
Nb	2	11	8	9	16	13	2	9	9
Zr	2	133	153	123	177	179	153	190	193
Y	1	28	26	20	36	31	35	25	34
La	11	66	16	19	42	39	52	19	35
Ce	5	62	47	56	87	82	98	45	72
Nd	5	26	22	24	34	34	39	22	31
Cr	3	225	294	209	265	256	253	350	176
Ni	3	164	83	115	130	155	99	123	185
V	3	120	75	106	140	134	72	105	147
Co	2	24	22	26	26	26	27	19	24
Cu	2	45	53	64	52	65	42	21	35
Zn	2	87	38	57	95	87	979	124	322
Pb	2	< 2	22	25	28	30	29	17	29
Sc	4	17	7	12	17	18	14	17	21
F	40	464	395	529	505	642	n.d.	n.d.	n.d.
Cl	3	325	26	27	41	55	n.d.	n.d.	n.d.
S	10	4630	39	< 10	217	180	n.d.	n.d.	n.d.

SED
5, 1511–1573, 2013

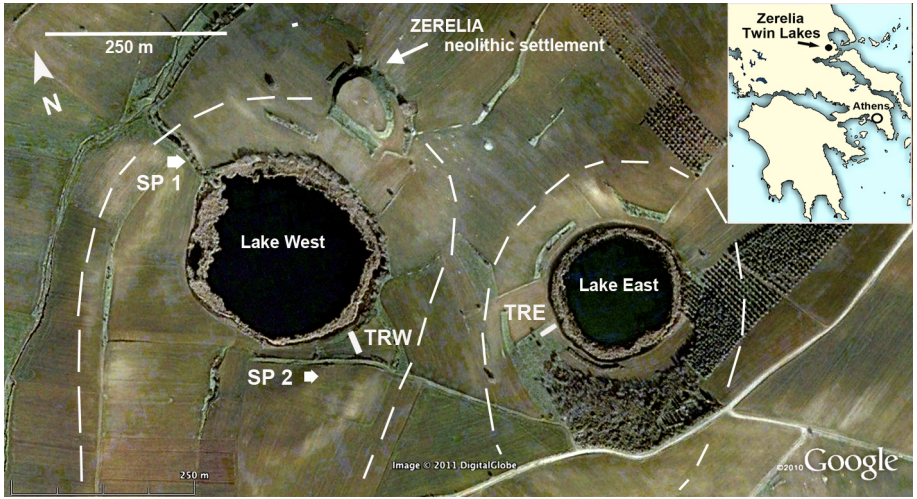

Fig. 1. The Magoula Zerelia twin-lakes (the larger Zerelia Lake West = ZLW and the smaller Zerelia Lake East = ZLE) in the agricultural fields SW of the town of Almiros (Thessaly, see insert) with the hill-site of the prehistoric Magoula Zerelia settlement. White dashed lines mark the distribution of the "polymict carbonate breccias". SP 1 and 2 mark sampling points in the southern shallow wall and at the embankment of the northern spill of the breccias; TRE and TRW are the localities of the 1 m wide and 7 m (TRE) and 8.8 m (TRW) deep trenches. Image 2011 Digital Globe Google Earth, date of imagery 1.7.2004; the triangulation point at Magoula Zerelia hill is at 39° 09′ 53.74 N, 22° 42′ 39.04 E at 148 m elevation.

SED
5, 1511–1573, 2013

Fig. 2. (a) The eastern Magoula Zerelia lake ZLE, 150 in diameter and 6 to 8 m depth, elevation a.s.l. 134 m (Fig. 1); **(b)** the western Magoula Zerelia lake ZLW, 250 m in diameter and 6 to 8 m, depth elevation 130 m (Fig. 1), in the background Othrys mountains.

SED
5, 1511–1573, 2013

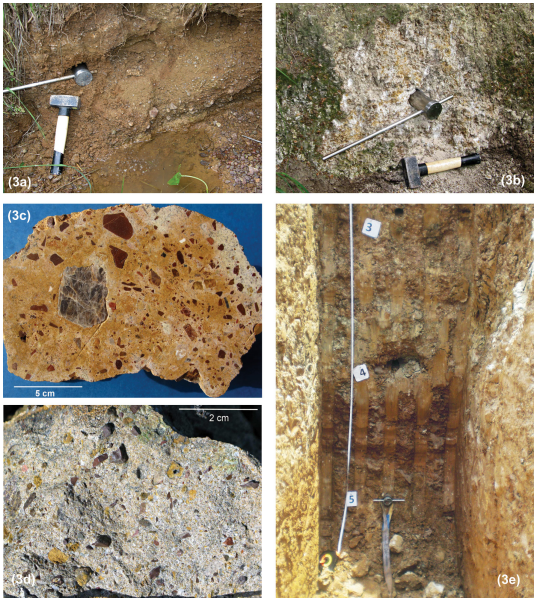

Fig. 3. (a) Outcrop at the sampling point (Sp1) in the shallow wall of the larger western lake. The upper 1 m consist of loose packed polymict breccia mainly consisting of reddish chert fragments and yellowish carbonate clasts without stratification and sorting. Common limestone and marly pebbles of the surrounding vicinity are absent. **(b)** Outcrop at the sampling point (Sp2) at the embankment of the northern spill. The upper 2 m consist of loose packed polymict breccia without stratification and sorting, mainly made up of whitish to yellowish carbonate fragment in a clay-rich, marly matrix. **(c)** Polymict breccia "Type A" from the walls of the larger westerly lake ZLW. Broken fragments of quartz (grey) and reddish to brownish radiolarian cherts (SiO_2) are distributed chaotically in a dense, cryptocrystalline to fine-grained calcite matrix with feathery and arborescent textures (Fig. 4e). **(d)** The less common yellow to light orange, non-porous polymict breccia "Type B" from ZLW (Fig. 6c and d), also rich in quartz and chert fragments. **(e)** Excavation of a 7 m deep and 1 m wide trench at the southwestern part of the embankment of the easterly lake ZLE (Fig. 1). The numbers refer to meters of depth.

SED
5, 1511–1573, 2013

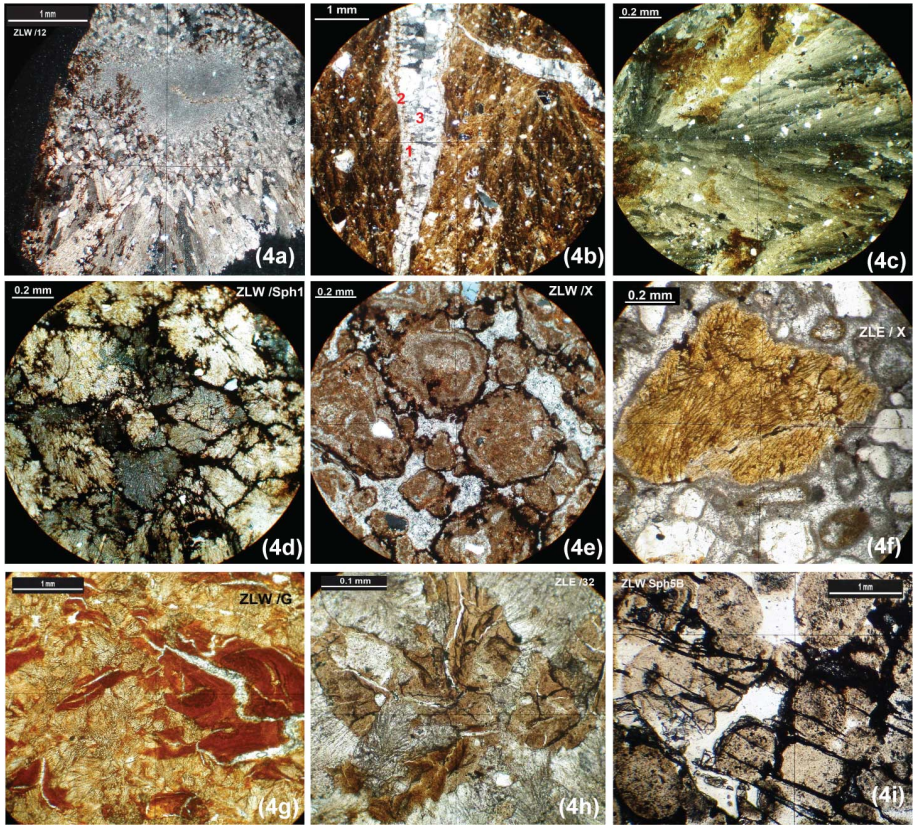

Fig. 4. Caption on next page.

SED
5, 1511–1573, 2013

Fig. 4. (a) Crossed-polarized light microphotograph from thin sections of a carbonatic sphere made up from feathery calcite aggregates in different dimensions, which seem to have crystallized out of submicroscopic cryptocrystalline calcite **(b)** Crossed-polarized light microphotograph of calcite veins within a carbonate clast crosscutting feathery calcite aggregates (yellow-brown), spotted with small quartz fragments (white), and showing three generations of crystallization (1) thin layer of fine feathery calcite grown perpendicular to the outer rim, (2) thin brownish calcite clay layer and (3) inner euhedral calcite filling. **(c)** Crossed-polarized light microphotograph of calcite crystals with "feathery textures" including micro fragments of quartz (white spots) as typical matrix in many brecciated clasts. **(d)** Crossed-polarized light microphotograph of calcite crystal patches with "feathery textures" as matrix of a sphere. Black interstitial fillings: cryptocrystalline iron and manganese oxides. **(e)** Crossed-polarized light microphotograph of a clast with carbonate spheroidal particles, which occur either as individual spheroidal particles or exhibit coalescent bounding in a euhedral calcite matrix. The spheroidal particles are made up of cryptocrystalline carbonates, partly showing feathery textures. **(f)** Plane-polarized light photomicrograph of a micro-breccia clast with spheroidal carbonate particles in a micro granular calcite matrix. Some of the particles contain quartz, other small carbonate feathery clasts. All particles exhibit microcrystalline carbonate rims. **(g)** Crossed-polarized light photomicrograph of irregular, dense "glass-shaped" reddish illite-kaolinite fragments in a yellowish calcite matrix with feathery textures and veins of granular calcite (see backscattered SEM images Fig. 6d and e); **(h)** Plane-polarized light photomicrograph of irregular, dense "glass-shaped" brownish clay fragments in a calcite matrix with feathery textures and veins of granular calcite. **(i)** Plane-polarized microphotograph of a quartz fragment made up of recrystallized quartz spheroidal particles of millimeter dimensions; the white interstitial matrix consists of cryptocrystalline and feathery quartz; black parallel cracks are filled with iron- and manganese oxides (Sph5B).

SED
5, 1511–1573, 2013

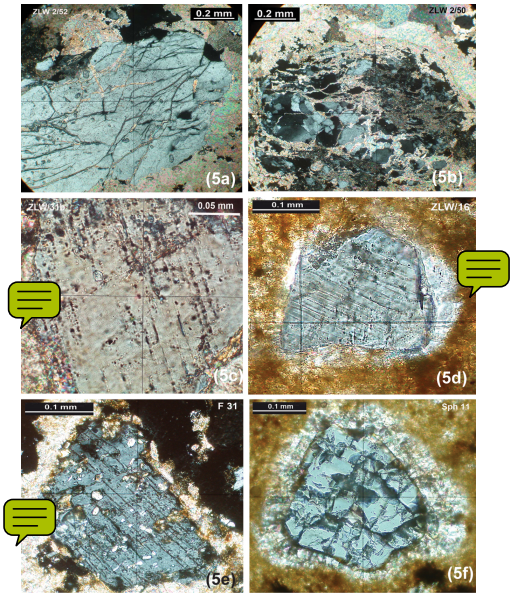

Fig. 5. Crossed-polarized light microphotographs from thin sections: **(a)** irregular fractures in a quartz fragment. **(b)** Brittle deformation of quartz with a network of calcite veins in a clast with patchy feathery calcite matrix. **(c)** Quartz as a fragment in a clast with micro-sparitic calcite matrix (sample Alm31, ZLW). Two sets of planar wide spaced decorated deformation fractures (PFs) are present, trending NNW-SSE and NE-SW. Directions are in relation to an arbitrary "north" at the top of the image. **(d)** Quartz fragment showing close spaced planar fractures in a dense, microcrystalline carbonate matrix (Sample Alm16). **(e)** Quartz fragment with a wide spaced set of planar fractures and spotted with calcite inclusions (sample F31). **(f)** Perpendicular fractured quartz fragment in a patchy feathery calcite matrix with calcite reaction rim with several small internally curved fractures indicating the existence of former gas bubbles (sample Sph11, spheroidal fragment).

SED
5, 1511–1573, 2013

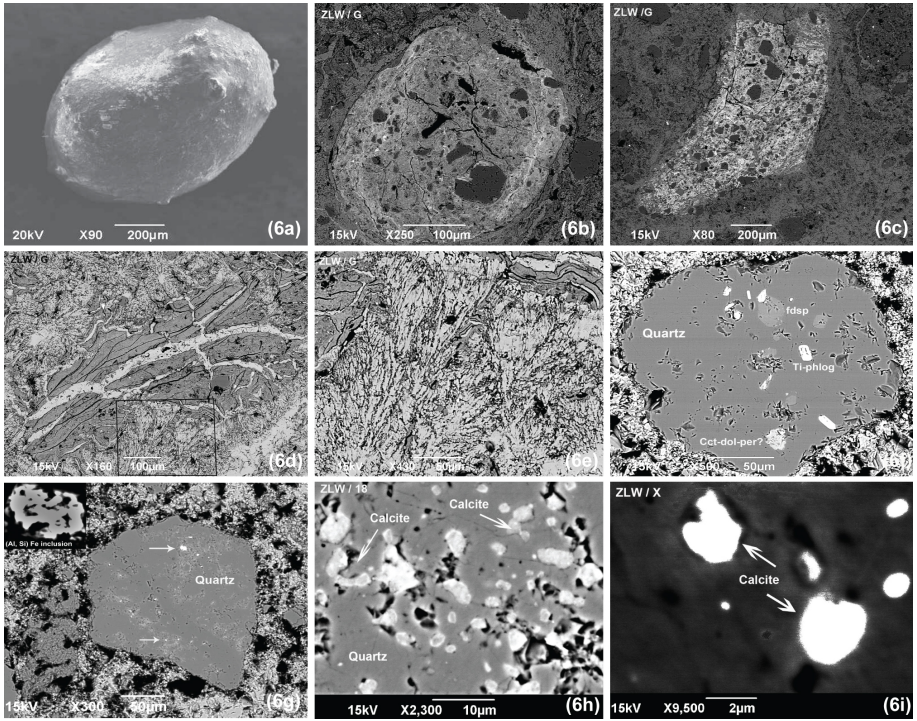

Fig. 6. Caption on next page.

SED
5, 1511–1573, 2013

Fig. 6. Backscattered electron images of spheroidal particles, "breccia-in-breccia" fragments, feathery carbonate matrix, and poikilitic quartz fragments from sampling point Sp1 (ZLW,): **(a)** polymict microbreccia spheroidal particle (see Fig. 6b and c). **(b)** Detailed image of a polymict spheroidal micro-breccia (a "breccia-in-breccia spherule") and its matrix (sample Alm G; chemical compositions are shown in Table 1. The carbonate-silicate "spherule" shows concentric rims and a microcrystalline silicate-carbonate core with quartz fragments surrounded by a feathery calcite matrix. **(c)** Same breccia clast as Fig. 5b with irregular "breccia-in-breccia" component, containing fragments of quartz, magnetite, and ilmenite with bulged shapes. **(d)** Relict decomposed glass fragment in a feathery calcite groundmass cut by calcite veins in feathery calcite matrix (see also Fig. 4g and h). **(e)** Detail in **(c)**: feathery calcite crystals, grey: dense "glass-shaped" reddish smectite fragments. **(f)** Quartz fragment with weak mosaic texture bearing inclusions of calcite-dolomite, uncertain periclase, alkalifeldspar, and phlogopite (sample AlmX). **(g)** Quartz in microcrystalline calcite matrix with (Al, Si) Fe inclusions; see detailed image box: Skeletal (Al, Si) Fe inclusion in quartz (polymict breccia, AlmX2). **(h)** Quartz fragment with mosaic texture containing innumerable globular Mg-bearing calcite inclusions with dimensions from nanometer scales to a few micrometer in sample Alm18. **(i)** Quartz fragment with inclusions and globules of dimensions from nanometer scales to a few micrometer (sample AlmX).

SED
5, 1511–1573, 2013

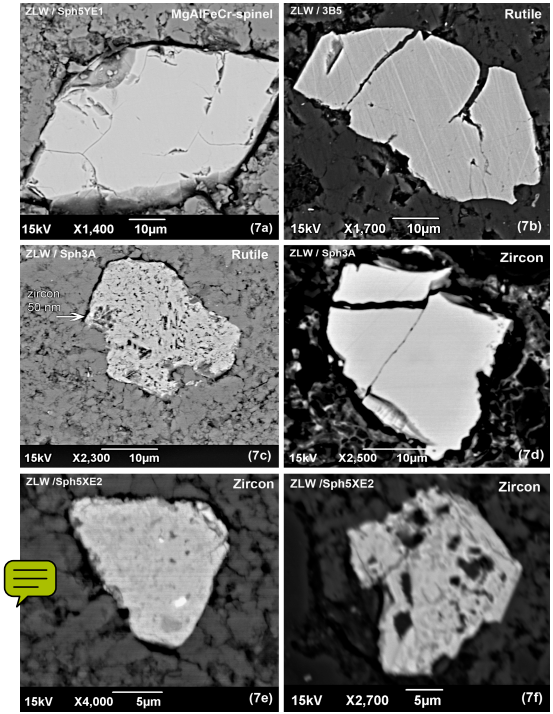

Fig. 7. Backscattered electron images of single crystals with irregular shapes and bulged rims: **(a)** Mg-Al-Fe chromspinel in microcrystalline carbonate matrix of a spheroidal particle. **(b)** Bulged rutile fragment in microcrystalline carbonate matrix. **(c)** Skeletal aggregate of rutile in "porcelain" like cryptocrystalline carbonate matrix, Sph5E6 with a nanometer sized zircon inclusion. **(d)** Zircon fragment with bulged and frayed rims, detail in carbonate sphere Sph3A. **(e)** Zircon with frayed rims and a blurred "granular" texture in "porcelain" like cryptocrystalline carbonate matrix. **(f)** Skeletal zircon with high uranium content in "porcelain" like cryptocrystalline carbonate matrix of a spheroidal particle.

SED
5, 1511–1573, 2013

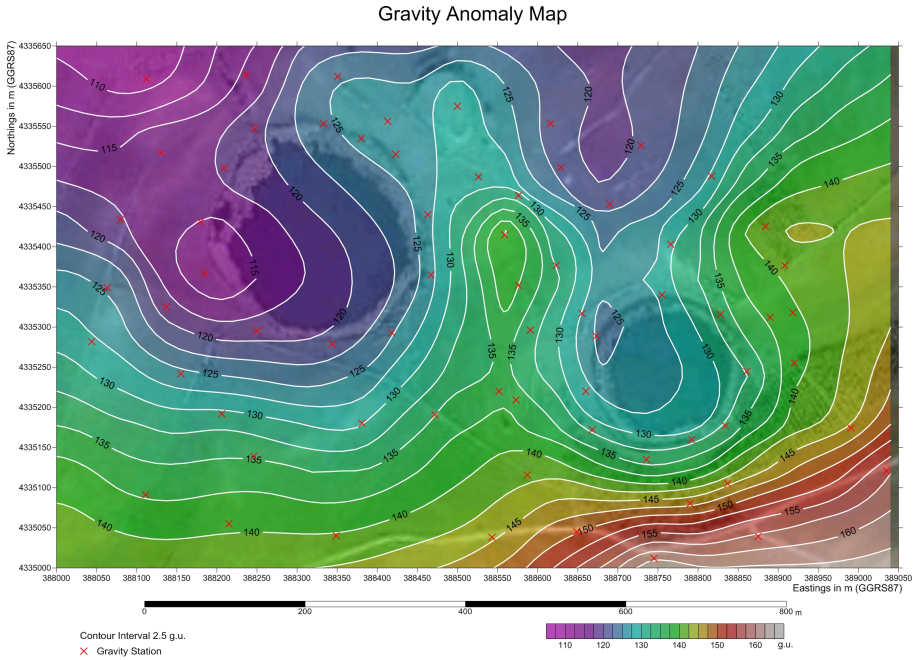

Fig. 8. The reduced Gravity Anomaly Map shows two gravity lows associated with the localities of the two lakes, reaching values of about 115 and 125 gravity units (gu).

SED
5, 1511–1573, 2013

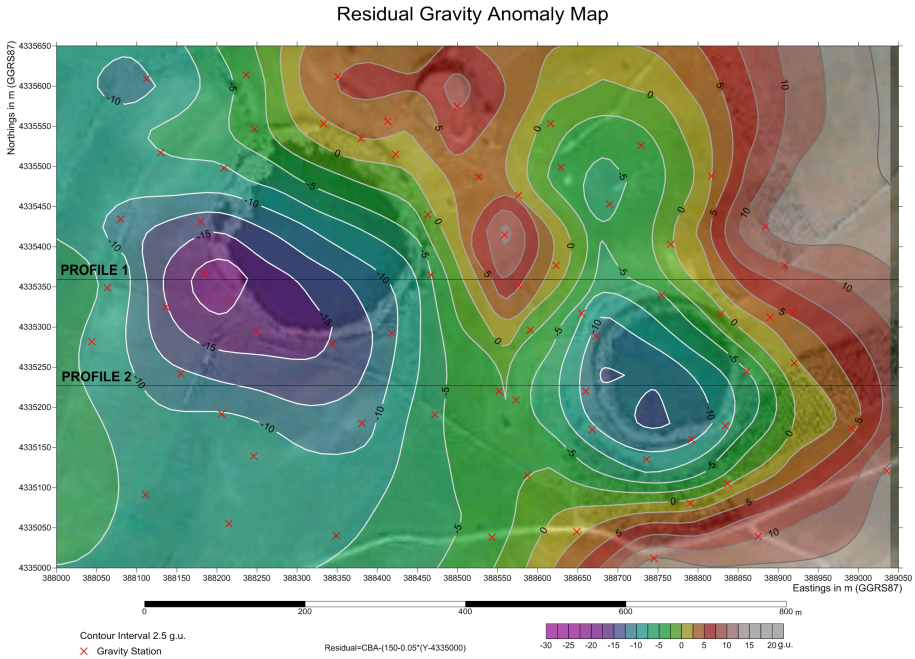

Fig. 9. Residual Gravity Anomaly Map (contour interval 2.5 gravity units) based on the IGSN'71 datum and GRF'67, superimposed over the Google image of the lakes area, and showing the lines of the two W–E profiles for modeling.

SED
5, 1511–1573, 2013

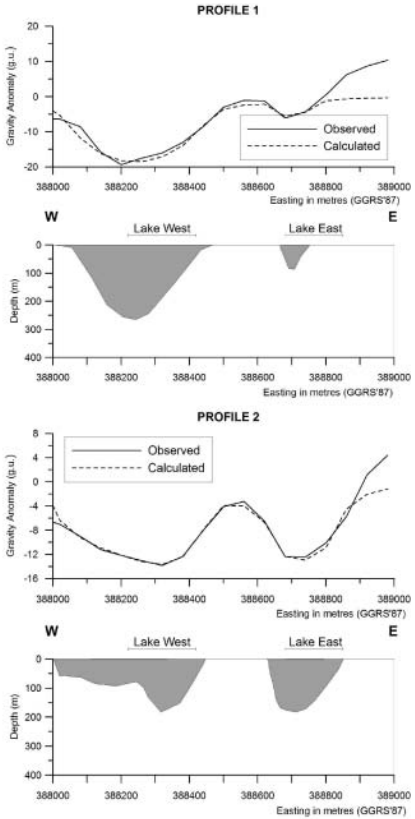

Fig. 10. (Upper Part) Modeling of the Residual Gravity E–W Profile 1 (Fig. 9) through the center of the western lake and through the northern part of the eastern lake; density contrast $-350\,\mathrm{kg\,m^{-3}}$. (Lower Part) Modeling of the Residual Gravity E–W Profile 2 (Fig. 9) through the center of the eastern lake and through the part of the western lake; density contrast $-350\,\mathrm{kg\,m^{-3}}$.

SED
5, 1511–1573, 2013

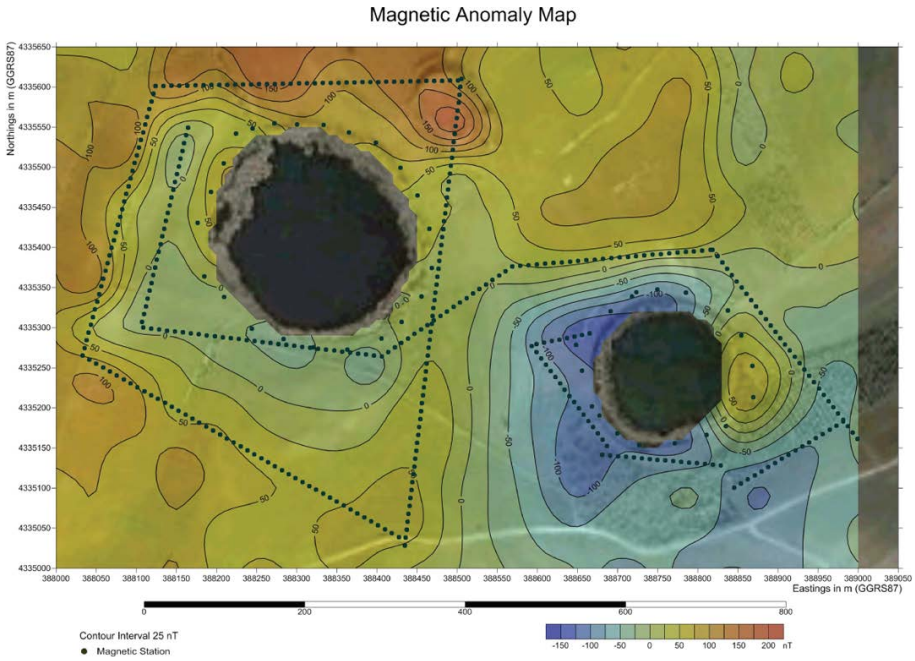

Fig. 11. Total field magnetic anomaly map (contour interval 25 nT), superimposed over the Google image of the lakes area.

SED
5, 1511–1573, 2013

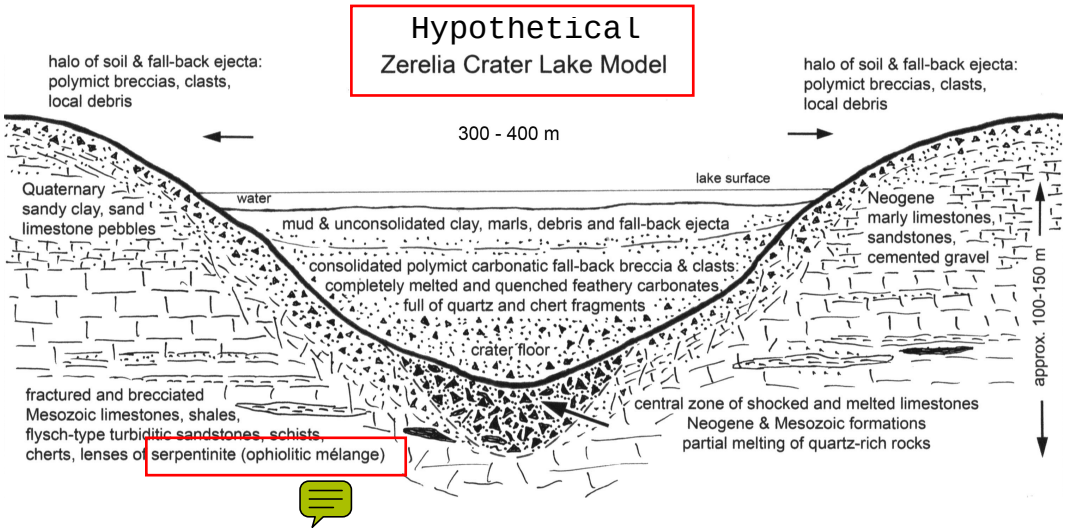

Fig. 12. Magoula Zerelia Crater Lake Model. Approximate dimensions of the larger westerly lake. The basement rocks below the true crater floor are fractured and brecciated but generally show no distinctive shock effects, except in a small zone (outlined by a stippled line) in the center of the structure containing possibly impact melts in form of small lenses. The crater is may be filled, to half its original height, with a variety of breccias. A layer of ejected material ("fall-back breccia") overlies the uplifted crater rim (halo) and proximal surroundings of the crater.

SED
5, 1511–1573, 2013